Evaluating Monin–Obukhov Scaling in the Unstable Oceanic Surface Layer

ZHIHUA ZHENG,[a,b] RAMSEY R. HARCOURT,[a,b] AND ERIC A. D'ASARO[a,b]

[a] *Applied Physics Laboratory, University of Washington, Seattle, Washington*
[b] *School of Oceanography, University of Washington, Seattle, Washington*

(Manuscript received 20 August 2020, in final form 26 November 2020)

ABSTRACT: Monin–Obukhov similarity theory (MOST) provides important scaling laws for flow properties in the surface layer of the atmosphere and has contributed to most of our understanding of the near-surface turbulence. The prediction of near-surface vertical mixing in most operational ocean models is largely built upon this theory. However, the validity of MOST in the upper ocean is questionable due to the demonstrated importance of surface waves in the region. Here we examine the validity of MOST in the statically unstable oceanic surface layer, using data collected from two open ocean sites with different wave conditions. The observed vertical temperature gradients are found to be about half of those predicted by MOST. We hypothesize this is attributable to either the breaking of surface waves, or Langmuir turbulence generated by the wave–current interaction. Existing turbulence closure models for surface wave breaking and for Langmuir turbulence are simplified to test these two hypotheses. Although both models predict reduced temperature gradients, the simplified Langmuir turbulence model matches observations more closely, when appropriately tuned.

KEYWORDS: Mixing; Wave breaking; Langmuir circulation; Surface layer

1. Introduction

Two major components of the Earth system, the ocean and the atmosphere, interact with each other through their own planetary boundary layers (PBLs), where the motions of fluids directly respond to the surface stress and buoyancy flux across the air–sea interface on time scales less than a day (Garratt 1992). Boundary layer processes are naturally relevant in many air–sea interaction problems [e.g., hurricanes (Emanuel 2003), Madden–Julian oscillation (Zhang 2005), El Niño (Dijkstra and Burgers 2002), etc.] and have great implications for accurate predictions of weather and climate. A comprehensive assessment of the role of the ocean and atmosphere in these problems requires a quantitative understanding of PBL dynamics, especially in terms of the vertical transports of momentum, heat and mass. These transports are largely carried by small-scale turbulent motions that must be parameterized in circulation models, due to limitations in computational capacity. The parameterization typically involves building approximations for turbulent fluxes, and using turbulence closure to estimate the effects of unresolved fluctuations upon the evolution of resolved mean fields. Informed by theories of molecular diffusion, early pioneers recognized that turbulent fluxes can be cast as functions of local mean gradients (Taylor 1915; Prandtl 1925; von Kármán 1931), and developing flux–gradient relationships has thus become an important approach in modeling boundary layer flows (Monin and Yaglom 1971).

Over the past 100 years, great progress has been made in the field of boundary layer meteorology (LeMone et al. 2019), and several similarity theories have been developed to provide scaling laws for statistical flow characteristics in the atmospheric boundary layer (ABL). In particular, the near-surface portion of the ABL, the surface layer, is the best understood, in part because measurements are easiest to make there, but also because its dynamics are relatively simpler, as a result of large turbulent Rossby number Ro ($\sim U/f|z|$, where U and $|z|$ are characteristic velocity and length scales, f is the Coriolis parameter) and nearly constant turbulent fluxes (Wyngaard 2010). Intrigued by such a well-defined problem, Monin and Obukhov (1954) proposed a similarity theory to delineate the vertical structure of an idealized atmospheric surface layer (ASL). Monin–Obukhov similarity theory (MOST) states that, under horizontally homogeneous and stationary conditions, every dimensionless scaling "group" in the surface layer is a universal function of the dimensionless height $\zeta = |z|/L$, the ratio of height $|z|$ to the Obukhov length (Obukhov 1946)

$$L = \frac{u_*^3}{\kappa B_0}, \tag{1}$$

where u_* is the friction velocity, $\kappa = 0.4$ is the von Kármán constant, and $B_0 = -\overline{w'b'}|_0$ is the near-surface buoyancy flux. The Obukhov length is negative (positive) in unstable (stable) conditions, and its magnitude is a rough estimate of the distance at which buoyancy production becomes dynamically important in the turbulent kinetic energy (TKE) budget relative to surface shear production.

Specifically, in the interest of the mean vertical structure of potential temperature θ, or horizontal velocity u, the dimensionless group for its vertical gradient is exclusively determined by ζ in the framework of MOST:

$$\frac{\frac{\partial \overline{\chi}}{\partial z}}{\frac{\chi_*}{\kappa|z|}} = \phi\chi(\zeta), \quad \chi = \theta, u. \tag{2}$$

Denotes content that is immediately available upon publication as open access.

Corresponding author: Zhihua Zheng, zhihua@uw.edu

DOI: 10.1175/JPO-D-20-0201.1

Here the overbar and prime denote time averaging and fluctuation, respectively; z is the upward vertical coordinate; $\chi_* = -\overline{w'\chi'}|_0/u_*$ is the fluctuation scale of flow variable χ with $\overline{w'\chi'}|_0$ being the near-surface kinematic flux of χ. For instance, the friction velocity $u_* = \sqrt{-\overline{w'u'}|_0} = \sqrt{\tau_w/\rho_0}$ is the fluctuation scale of horizontal velocity u, where the reference seawater density $\rho_0 = 1025\,\mathrm{kg\,m^{-3}}$, w is the vertical velocity, and the x axis is chosen to align with the surface wind stress τ_w. The dimensionless gradient, or universal function ϕ_χ represents the effects of buoyancy on turbulence, relative to the law-of-the-wall scaling (von Kármán 1931) for an unstratified surface layer ($\zeta = 0$). Numerous experimental efforts, both over land (e.g., Businger et al. 1971) and sea surface (e.g., Edson et al. 2004), have gone into determining the functional form of ϕ_χ for practical application. Many different analytic forms have been suggested in a voluminous body of literature (reviewed in Högström 1996; Foken 2006). Almost all empirical curves are similar in unstable conditions, while some disparities are common for expressions in stable conditions, presumably as a consequence of the intermittent and weak turbulence under stable stratification (Mahrt 2014). The widely accepted set of universal functions for momentum ϕ_m and heat ϕ_h is based on the Kansas experiment (Businger et al. 1971), from which particularly homogeneous and steady conditions and well-measured data were optimized to give

$$\phi_m = 1 + 4.7\zeta, \quad \phi_h = 0.74 + 4.7\zeta, \quad 0 < \zeta < 1; \tag{3a}$$

$$\phi_m = (1 - 15\zeta)^{-1/4}, \quad \phi_h = 0.74(1 - 9\zeta)^{-1/2}, \quad -2 < \zeta < 0. \tag{3b}$$

MOST has been generally successful in describing the flux–profile relationships in the ASL over a moderate range of ζ [as shown in Eqs. (3)]. It also laid a solid foundation for the later establishment of bulk transfer relations (the COARE algorithm; Fairall et al. 1996, 2003), since its formulation implicitly suggests a parameterization for turbulent fluxes:

$$\overline{w'\chi'}|_0 = \frac{-u_*\kappa|z|}{\phi_\chi(\zeta)}\frac{\partial\overline{\chi}}{\partial z} = -K_\chi\frac{\partial\overline{\chi}}{\partial z}. \tag{4}$$

In this case, the turbulent flux and the gradient are related via a simple, stability-dependent eddy diffusivity $K_\chi = u_*\kappa|z|/\phi_\chi$. Thus far, many atmospheric models still rely on this method to deduce surface fluxes from near-surface mean profiles.

The ocean surface boundary layer (OSBL) mirrors its atmospheric counterpart in many ways, and its representation in circulation models also shares many features with the ABL. By analogy to the atmosphere, vertical mixing schemes for the OSBL also draw on knowledge from MOST. For example, the widely used K-profile parameterization (KPP; Large et al. 1994) employs the universal function ϕ_χ to account for buoyancy effects in formulating a "turbulent velocity scale w_χ," and judiciously extends the surface layer scaling to the rest of the OSBL. Although not explicitly related to MOST, other higher-order schemes (e.g., Mellor and Yamada 1982; Kantha and Clayson 1994; Rodi 1987) were also tuned to match the surface layer similarity relations [Eqs. (3)] in a simplified framework (see appendix C). The incorporation of MOST in ocean models did improve their predictive capacity to some extent, however, considerable model errors still occur in many cases (e.g., too shallow mixed layer in the Southern Ocean; Sallée et al. 2013). Some of these errors are potentially related to the assumption that the surface layer of the ocean can be characterized by the same scaling law as the ASL.

Not surprisingly, as the community becomes more aware of the dynamical impacts of surface gravity waves, suspicion arises about the validity of Monin–Obukhov scaling in the OSBL (Sullivan and McWilliams 2010). Meanwhile, measurements of fluxes and gradients reported from coastal waters near Martha's Vineyard (Gerbi et al. 2008) have already shown signs of invalidation.

In fact, the turbulence in the upper layers of the ocean and the consequent vertical mixing are inevitably affected by surface waves. Close to the surface, waves break intermittently as they propagate rapidly. One important effect of wave breaking is the downward injection of kinetic energy as turbulence. The classical law-of-the-wall scaling predicts the turbulence dissipation rate $\varepsilon \sim u_*^3/\kappa|z|$ in a neutral surface layer. However, near-surface measurements of ε in the ocean under strong wind and weak buoyancy forcings (Agrawal et al. 1992; Drennan et al. 1996; Terray et al. 1996) repeatedly give much higher magnitude of ε than the classical prediction, and exhibit a more complicated, three-layer structure of ε: Within about one significant wave height (H_s) of the surface, ε is large and more or less constant; Below that, ε decays much faster than the -1 power-law before eventually resuming the classical scaling at deeper depths.

A second effect results as the Lagrangian-mean wave velocity, the Stokes drift, induces the Craik–Leibovich (CL) vortex force (Craik and Leibovich 1976) and additional material transport to generate Langmuir circulations, cells, or turbulence that fill the entire OSBL. Conceptually, they can be viewed as arrays of counterrotating vortices with elongated major axes oriented roughly downwind (Sullivan and McWilliams 2010). Oftentimes, one can identify them by streaks of buoyant debris on the surface (Langmuir 1938), and by bubble clouds trapped beneath these streaks using side-scan sonar (e.g., Thorpe 1984; Zedel and Farmer 1991). Although turbulence measurements in strongly convective OSBL have generally supported Monin–Obukhov scaling (Shay and Gregg 1986), available field observations under strong wind conditions did show some deviations from the ABL (D'Asaro 2014). First, the bulk average of the vertical TKE $\overline{w'w'}$ (D'Asaro et al. 2014), and dissipation rate (Lombardo and Gregg 1989; Carniel et al. 2012) all seem to be higher than expected from classical scaling. Second, the ordering of turbulent velocity variances observed in shallow-water environment (Gargett and Wells 2007) shows much stronger crosswind and vertical components than typical shear-driven turbulence, in which the velocity fluctuations are dominantly downwind. These differences are likely due to Langmuir turbulence, as large-eddy simulation (LES) techniques can consistently predict these distinct features when the CL vortex force is included (e.g., Skyllingstad and Denbo 1995; McWilliams et al. 1997; Tejada-Martínez and Grosch 2007; Harcourt and D'Asaro 2008; Kukulka et al. 2012). In stabilizing forcing conditions, Langmuir turbulence has also been found to inhibit the restratification and hence

invalidates Monin–Obukhov scaling (Kukulka et al. 2013; Pearson et al. 2015).

As extra physics is introduced by processes related to surface waves, the surface layer of the ocean is expected to be dynamically different from the ASL. The canonical similarity theory with scaling parameters $|z|$, L, u_*, and χ_* may become inadequate to encapsulate the relevant dynamics. Thus, it is incumbent upon us to examine the applicability of such flux–gradient relationships in the oceanic surface layer.

In this paper, we evaluate the validity of MOST in a surface wave-affected oceanic surface layer, using data collected from two open ocean sites. The rest of this manuscript is organized as follows. In section 2, we introduce the in situ measurements and data analysis, and compare observations to the predictions by MOST. In section 3, we consider two hypotheses for the theory-observation discrepancies: one attributes the differences to surface wave breaking, and the other, to Langmuir turbulence. Each hypothesis is tested using a simplified turbulence closure model, and the model results are also compared to observations. Finally, a brief summary is presented in section 4.

2. Observations

The evaluation of MOST flux–gradient relationships requires accurate measurements of surface fluxes and mean profiles in a quasi-steady surface layer. Datasets considered in this study are from two open ocean taut-line moorings (Fig. 1). The subsurface sensors are assumed to have been sampling upper-ocean properties at their nominal depths. At both mooring sites, oceanic conductivity–temperature measurements are complemented by concurrent recordings of surface waves and a variety of surface observations for estimating air–sea fluxes, including winds, incoming solar and longwave radiation, rain, air temperature, relative humidity, and barometric pressure.

The first dataset (Cronin 2007) is from a long-term time series site, the Ocean Climate Station Papa (OCSP, nominally at 50.1°N, 144.9°W) in the northeastern Pacific. It has long been an attractive natural laboratory for boundary layer studies because of the weak lateral processes there. During active periods, the OCSP mooring is instrumented with sensors to measure subsurface temperature and conductivity once every 10 min. The meteorological sensors mounted above the buoy have higher sampling rates, usually 1 or 2 Hz, but the recorded resolutions vary from 1 to 10 min. Hourly data were created by applying Hanning filters to the original records (Anderson et al. 2018). Since 2010, a Datawell Waverider buoy has also been deployed near the OCSP mooring to report directional surface wave spectrum every 30 min (Thomson 2019). To have simultaneous hydrographic, meteorological and surface wave measurements, data from OCSP are truncated to a time period from June 2010 to November 2019.

The second dataset (Farrar 2015) was collected during the field campaign of the first Salinity Processes in the Upper-Ocean Regional Study (SPURS-I; Lindstrom et al. 2015; Farrar et al. 2015). As part of the monitoring array in the subtropical North Atlantic (approximately 24.5°N, 38°W), a surface buoy was deployed in September 2012 and recovered in September 2013. The SPURS-I mooring carried similar meteorological sensors to measure meteorological conditions once per minute and transmit hourly averages via satellite. Below the surface, the mooring line was equipped with a denser array of sensors (~1 m spacing in upper 10 m) for temperature and conductivity measurements in every 5 min. In addition, the buoy also had an instrument to measure the height and direction of surface waves by recording the angular accelerations of pitch, roll and yaw, as well as the vertical heave (Bouchard and Farrar 2008). These raw data were later processed by J. T. Farrar (2014, unpublished data) to produce hourly records of directional surface wave spectrum.

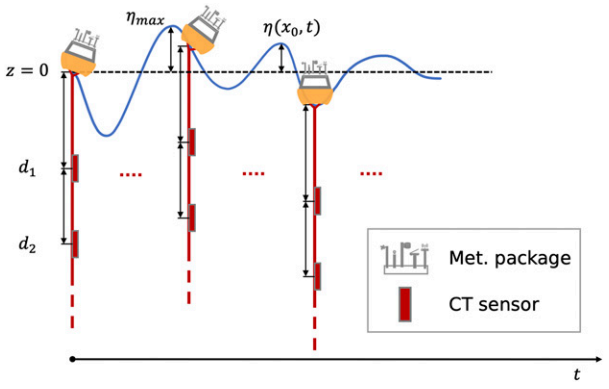

FIG. 1. A sketch for typical taut-line mooring setup that measures oceanic conductivity–temperature (CT) and meteorological conditions over sea surface. Hourly averaged data are used to investigate the response of oceanic surface layer to surface forcing. Sensor's nominal depth along the mooring line, referenced to the mean sea surface ($z = 0$), is treated as the measurement distance from the surface.

For both datasets, the profile of Stokes drift velocity $\mathbf{u}^s$ and its vertical shear are estimated from the directional wave spectrum, following the method described in appendix A. Surface wind stress, surface heat, and salt fluxes were estimated using the TOGA COARE 3.0 algorithm (Fairall et al. 2003) from measured meteorological variables (see details about the flux calculations at OCSP on https://pmel.noaa.gov/ocs/flux-documentation). Considering the penetrative effect of shortwave radiation I, the buoyancy flux to a layer of depth $|z|$ is computed following Large et al. (1994):

$$B_f(z) = B_0^t + [B^r(0) - B^r(z)], \tag{5}$$

where B_0^t is the turbulent component of the buoyancy flux due to sensible heat flux, latent heat flux, net downward longwave radiation and salt flux at the surface; B^r is the radiative component that decays with depth. The sign convention for B_f is positive (negative) when the buoyancy flux is into (out of) the ocean. The radiative component B^r is modeled by a two-band exponential profile (Paulson and Simpson 1977):

$$B^r(z) = \frac{\alpha g I_0}{\rho_0 c_p}\left[r_s e^{z/\mu_1} + (1 - r_s)e^{z/\mu_2}\right], \tag{6}$$

TABLE 1. The Jerlov water type and corresponding constants assumed in this study.

Site	Jerlov water type	r_s	μ_1 (m)	μ_2 (m)
OCSP	II	0.77	1.5	14
SPURS-I	IB	0.67	1.0	17

where I_0 is the net downward shortwave radiation at the surface, α is the thermal expansion coefficient of seawater, g is the gravitational acceleration, and c_p is the specific heat at constant pressure. Here, the solar spectrum is divided into two wavelength bands, with fraction r_s and $1 - r_s$ of the total radiation. Each band decays exponentially with a characteristic e-folding length scale μ. The values of r_s, μ_1, and μ_2 depend on the Jerlov (1976) water type. Based on a global climatology of water optical properties (Simonot and Le Treut 1986), water type II and IB are assumed for OCSP and SPURS-I, respectively (Table 1). The depth-dependent buoyancy flux B_f is used to calculate the Obukhov length, as the buoyancy force experienced by seawater changes with depth. This treatment of the solar radiation is one of the simpler possible formulations, but any limitation of this approach is not likely to have a big impact on our following results, since most data selected are from nighttime (section 2a).

a. Mean temperature profiles and vertical gradients

For consistency, time series with resolution finer than hourly are averaged in 1-h intervals. As the salinity measurements are more susceptible to sensor drift (see appendix B) and the accuracy is not as high as temperature (±0.002°C), they are only used to determine density for the purpose of identifying the boundary layer depth H. Only temperature data are directly used in the validation of MOST. At first glance, the temperature profile may seem smooth, but if one zooms into the surface layer, small-scale serrations are almost ubiquitous (Fig. 2), probably owing to the different thermal responses of sensors. To reduce theses noises and extract the mean thermal stratification, we follow the standard method in atmospheric studies (Businger et al. 1971) to fit every temperature profile with a second-order polynomial function in logarithmic space:

$$\overline{\theta}(z) = p_2(\ln|z|)^2 + p_1 \ln|z| + p_0, \tag{7}$$

where p_0, p_1, and p_2 are the polynomial coefficients. The logic behind this logarithmic fit is that the profile of any mean

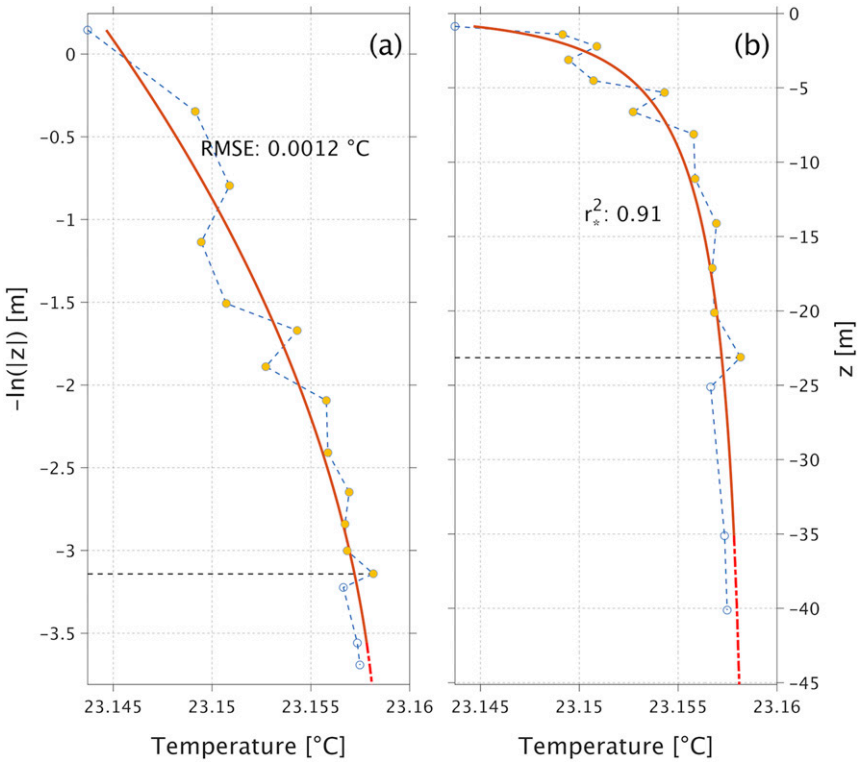

FIG. 2. An example from SPURS-I shows the second-order polynomial fit [Eq. (7)] of temperature profile. The original profile (blue dash line with circles), taken from 0330 local time 10 Feb 2013, is shown in both (a) logarithmic and (b) linear coordinates. The solid red line shows the best fit using data within the depth range it covers. The dash–dotted red line shows the extrapolated polynomial function outside the fitting range. Surface layer depth ($0.2H$) is indicated by the horizontal black dash line. Solid yellow circles mark the depths where dimensionless gradients are computed; r_*^2 is the goodness of fit adjusted for the degrees of freedom.

quantity in the surface layer is expected to vary logarithmically with height (depth) in neutral conditions, while in nonneutral conditions, the profile is usually slightly curved in the logarithmic coordinate (Panofsky 1963). For each temperature profile, multiple second-order polynomial fits are conducted within the depth range of $[0, 0.3H]$, using various numbers of data points. Three criteria are required for a fit to be considered as good: 1) the first- and second-order vertical derivatives are monotonic functions; 2) the root-mean-square error (RMSE) is less than 0.002°C; 3) after adjusting for degrees of freedom, the coefficient of determination (r^2) is larger than 0.5. Among all the good fits for a profile, we pick the best one, if there is any, that has the smallest RMSE. If no best fit can be found, then the profile is excluded from the analysis. In total, about 89% and 54% of the profiles are excluded in OCSP and SPURS-I datasets, respectively, either due to the lack of robustness of fits (17% and 16% in unstable conditions, 12% and 27% in stable conditions), or insufficient data in the surface layer. The best fitting function is used to calculate temperature gradients and ϕ_h at different levels z_i:

$$\frac{\partial\overline{\theta}}{\partial z}=\frac{(2p_2\ln|z_i|+p_1)}{z_i}, \tag{8a}$$

$$\phi_h=\frac{\dfrac{\partial\overline{\theta}}{\partial z}}{\dfrac{\theta_*}{\kappa|z_i|}}, \tag{8b}$$

where θ_* is computed using the heat flux that includes depth-varying solar radiation. Considering the uncertainty of derivatives at the two ends of the fitting range, temperature gradients are only calculated at the interior depths of the fitting range, but still within the surface layer (Fig. 2). This also diminishes the effect of flow distortion on temperature gradients, as the first temperature measurement below the surface usually contains a signal from seawater at shallower depth, due to the distortion of near-surface flow by the buoy.

b. Surface layer depth

Departing from the ASL convention, which considers the lower 10% of the ABL, we treat the upper 20% of the OSBL as the surface layer. The depth of the OSBL is determined as the shallowest level where the linearly interpolated bulk Richardson number Ri_b reaches a critical value Ri_b^c. In the absence of reliable near-surface velocity measurements at the moorings considered here, buoyancy profiles are used to define a bulk Richardson number in reference to a neutral logarithmic shear profile, computed at each level z_i as

$$\mathrm{Ri}_b(z_i)=\frac{(b_1-b_i)(z_1-z_i)}{|\mathbf{u}_1-\mathbf{u}_i|^2}\approx\frac{\kappa^2(b_1-b_i)(z_1-z_i)}{u_*^2\ln^2\left(\dfrac{z_i}{z_1}\right)}, \tag{9}$$

where $b=-g(\rho-\rho_0)/\rho_0$ is the buoyancy computed from local potential density ρ, and subscript 1 denotes quantity measured at the first sensor depth. Due to substantial sensor drifts, the salinity measurements from the SPURS-I mooring are calibrated (see appendix B) before calculating potential density. Different values of Ri_b^c are tested, and the optimal one is chosen to have the best coincidence with the mixed layer depth diagnosed from the $0.03\,\mathrm{kg\,m^{-3}}$ criterion (de Boyer Montégut et al. 2004). The resulting Ri_b^c for OCSP and SPURS-I are 0.85 and 2.30, respectively. Since the bulk Richardson number here is defined with an idealized velocity shear, it is not surprising to arrive at a critical value different from traditional values. The computed surface layer depths are used to confine the domain of our analysis and minimize uncertainty in the scaling results. However, the surface layer tends to be very shallow (a few meters) during daytime, so the majority the data used comes from unstable situations, often during nighttime.

c. Quasi-steady state

The turbulence in the OSBL can be nonstationary due to diurnal variations of atmospheric forcing; it can also be inhomogeneous in the horizontal as surface properties vary spatially. However, if the time and length scales of the OSBL are small relative to those of the external forcing, the OSBL may be considered as quasi-steady and horizontally homogeneous. Oftentimes, the boundary layer depth H and the large-eddy turnover time T_H are regarded as the internal length and time scale of the OSBL. The boundary layer eddies driven by the wind and surface buoyancy loss can be characterized by velocity scales u_* and w_*. The larger of these two is used to determine the turnover time here:

$$T_H=\frac{H}{\max(u_*,w_*)}, \tag{10}$$

where $w_*=(-HB_0)^{1/3}$ is the free-convection velocity scale (Deardorff 1970) that is set by the boundary layer depth and near-surface buoyancy flux. The external forcing changes as the wind stress, or buoyancy flux varies with time. The time scale of each forcing is estimated as the ratio of the forcing magnitude to the temporal rate of change:

$$T_W=\left|\frac{\tau_w}{\dfrac{\partial\tau_w}{\partial t}}\right|, \tag{11a}$$

$$T_B=\left|\frac{B_0}{\dfrac{\partial B_0}{\partial t}}\right|. \tag{11b}$$

Therefore, we define a period when the time scales of both wind stress T_W and buoyancy flux T_B exceed 10 times the large-eddy turnover time T_H as the quasi-steady period. An example of such selection is given in Fig. 3. As for the condition of horizontal homogeneity, we argue that the spatial scales of horizontal variability at both sites are much larger than the thickness of the OSBL (~100 m), so that the OSBL turbulence does not feel the effect of horizontal heterogeneity. These boundary layer approximations, including the quasi-steady state and horizontal homogeneity, are also assumed in our later simplification of PBL models (appendix C and section 3).

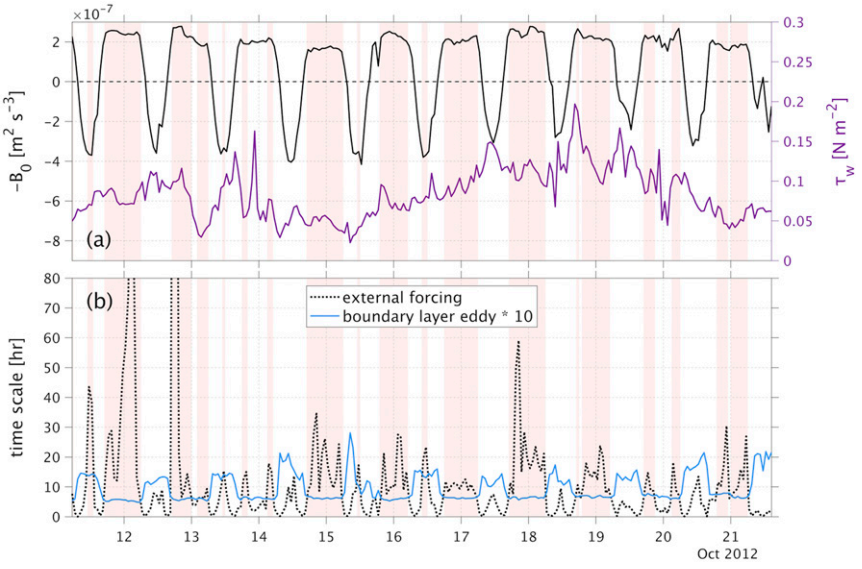

FIG. 3. An example from SPURS-I shows the selection of quasi-steady periods. (top) Time series of the near-surface buoyancy flux B_0 (black) and wind stress τ_w (purple) for about 10 days. (bottom) Time scale of external forcing (black, includes buoyancy and wind forcings) and 10 times that of the boundary layer eddy (blue). The quasi-steady period (vertical red shading) is reached when the time scale of external forcing exceeds 10 times that of the boundary layer eddy.

d. *Comparison of Monin–Obukhov scaling with observations*

According to MOST, the temperature difference between any two levels z_i, z_j in the surface layer should be

$$\Delta\overline{\theta}_{ij} = \overline{\theta}(z_i) - \overline{\theta}(z_j) = \int_{z_j}^{z_i} \phi_h \left(\frac{|z|}{L}\right) \frac{\theta_*}{\kappa|z|}\, dz, \qquad (12)$$

where $|z_i|$ and $|z_j|$ are the nominal sensor depths along the mooring line, and the universal function ϕ_h used here is based on the results [Eqs. (3)] from the Kansas experiment. These theoretical predictions of temperature difference are computed through trapezoidal numerical integration and are compared to those directly calculated from the fitted profiles. The comparison (Figs. 4a,c) shows that the observed temperature gradients are about half of the theoretical predictions, over most of the observed range of $\Delta\overline{\theta}$. This is robust at both sites, and is not subject to either the selection of quasi-steady periods in section 2c, or the profile fitting in section 2a. More intuitively, the juxtaposition (Figs. 4b,d) of the observed profiles and the MOST-predicted profiles also indicates that the ocean has weaker thermal stratification in the surface layer than the atmosphere, or than that predicted by MOST.

The distribution of the observed dimensionless temperature gradient ϕ_h in ζ is shown in Fig. 5. Again, the smaller observed values of ϕ_h below the Kansas curve are consistent with the smaller linear regression slopes (less than 1) in Figs. 4a and 4c. The deviation of the observations from the Kansas curve decreases as $|\zeta|$ increases, indicating that the failure of MOST mainly happens in the forced convection regime ($-1 < \zeta < 0$). Looking more closely, the different linear regression slopes (Figs. 4a,c) at these two sites, and the disparity of ϕ_h values in the same ζ bin (Fig. 5) may imply that the ϕ_h in oceanic surface layer does not only depend on ζ, and that other forcing parameters not considered in MOST might be important in setting the near-surface temperature gradients. Moreover, in the surface layer, smaller dimensionless temperature gradients suggest larger thermal diffusivity, as K_h is inversely proportional to ϕ_h [Eq. (4)]. These observational evidences clearly show that the classical Monin–Obukhov scaling for temperature is not appropriate for direct application in the unstable oceanic surface layer. This is a major finding of this study and the rest of this paper seeks to identify what process is responsible for the weaker thermal gradients, by considering surface waves.

3. Hypotheses testing

The reduced temperature gradients in the unstable oceanic surface layer naturally leads to the question of why the ocean is different from the atmosphere in this regard. As mentioned earlier, surface waves related processes can modify OSBL dynamics significantly, but they are not included in the current form of MOST. Therefore, we consider two hypotheses to explain the discrepancies between observations and MOST: 1) surface wave breaking is responsible for the observed weak temperature gradients, and 2) Langmuir turbulence is responsible for the observed weak temperature gradients. Although our current understanding of these two processes is still incomplete, attempts have been made to incorporate them into models for the PBL. Encouragingly, models with surface wave breaking (Craig and Banner 1994; Burchard 2001) have shown some skill in reproducing the near-surface dissipation

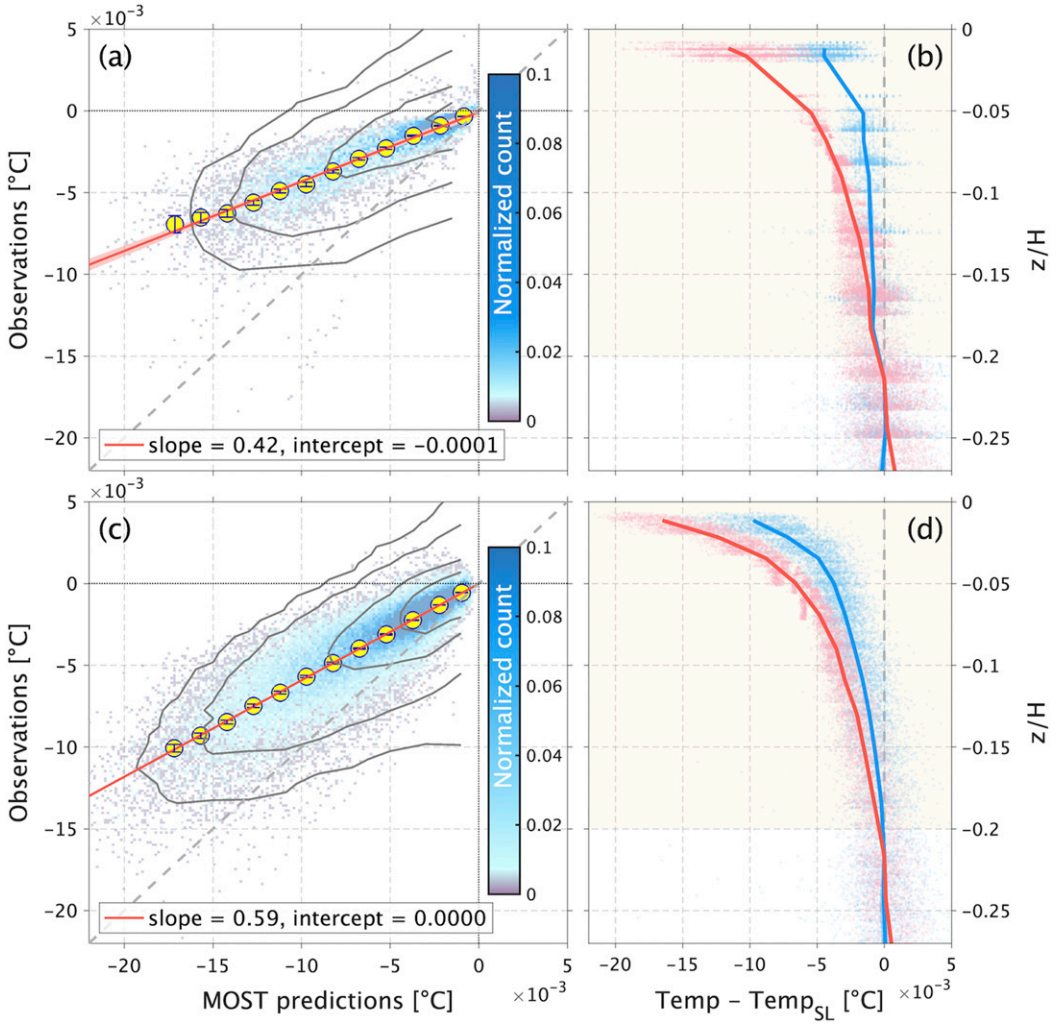

FIG. 4. Comparisons between observations and MOST predictions of surface layer temperature. (a) Observed vertical temperature differences $\Delta\overline{\theta}$ at OCSP vs those predicted by MOST. Scatter uses $\Delta\overline{\theta}$ from fitted profiles during quasi-steady periods, while probability contours for 30%, 60%, 90%, and 96% of distribution use $\Delta\overline{\theta}$ from all original profiles. Color of scatter represents data density, yellow circles show bin averages of scatter with 95% confidence intervals (error bars), and red line shows the linear fit of bin averages. (b) Observed temperature profiles (blue) vs those predicted by MOST (red). Predictions are obtained by cumulatively integrating the predicted gradients with ϕ_h from Eqs. (3). Temperatures are referenced to "Temp$_{SL}$," the mean values in the surface layer (area shaded yellow). Solid lines are ensemble averages of individual profiles (dots). Only profiles with boundary layer deeper than 50 m are used. For better visual comparison, profiles have been shifted to make the ensemble averages zero at the surface layer depth. (c),(d) As in (a) and (b), but use data from SPURS-I.

measurements under breaking waves, and models including Langmuir turbulence were found to better predict observed vertical TKE profiles (Harcourt 2015). Given the success of existing models in representing these two processes, we will take them as the approach for hypotheses testing.

The PBL models adopted here are commonly termed as second moment closures (SMCs), and use solutions of second-order turbulence statistics to inform the turbulent diffusivity in closing mean equations. In view of the relatively simple dynamics in the surface layer, a full SMC can be accordingly simplified to a superequilibrium version, where turbulence production is locally balanced by dissipation. Classical SMCs (e.g., Mellor and Yamada 1982; Kantha and Clayson 1994) with no explicit consideration of surface wave effects, when reduced to the superequilibrium version, are known to have independent temperature and momentum scalings that are very similar to MOST. An example for the derivation of model intrinsic similarity relations from Kantha and Clayson (1994) is given in appendix C. Also, full SMCs have been shown to approximately follow Monin–Obukhov scaling in steady states when constant forcing is imposed (Burchard et al. 1998). However, for a SMC that includes surface wave effects, we expect that the model-derived temperature and momentum scalings would deviate from MOST.

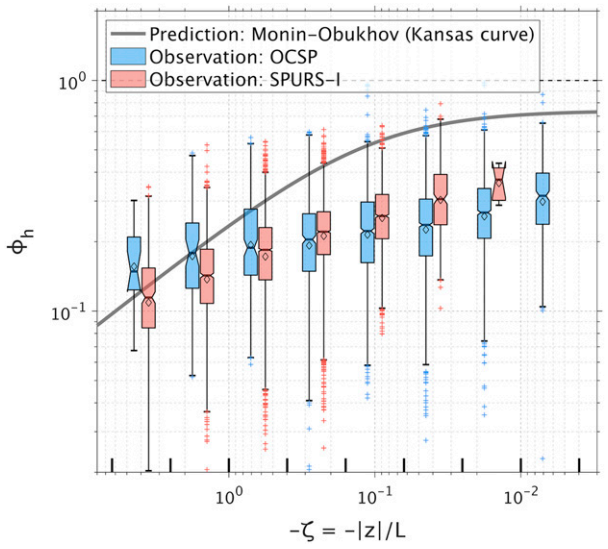

FIG. 5. Distribution of the observed dimensionless gradient ϕ_h in ζ space. Only data from quasi-steady periods are used. Dimensionless gradients from fitted profiles are grouped into logarithmically spaced bins (see vertical bars at the bottom). The paired boxes are horizontally offset from the bin center to show the distribution of $\log_{10}(\phi_h)$ from OCSP (blue) and SPURS-I (red) in the same ζ bin. On each box, the central mark indicates the median; the diamond indicates the mean; the top and bottom box edges show the upper and lower quartiles, respectively; the whiskers show the 99th and 1st percentiles; and the notch shows the comparison interval of the median. Medians of the ϕ_h from OCSP and SPURS-I are deemed different at the 5% significance level if their intervals do not overlap in the same bin. Data beyond whiskers are plotted as "+" symbols. The empirical relationship [Eq. (3b)] from the Kansas experiment (Businger et al. 1971) is displayed as the thick gray curve.

a. Similarity relations in surface wave breaking model

Craig and Banner (1994) presented the first of many models including the effects of surface wave breaking. They modified the classical Mellor and Yamada (1982) level-2.5 model by adding a down-the-gradient flux of TKE from the dissipated wave energy, which was assumed to be in proportion to u_*^3. Their model is successful in reproducing the high dissipation and the elevated decay with depth, but the analysis and model–observation comparison were conducted for a neutral boundary layer. In more general scenarios, buoyancy is also important for turbulence; hence we similarly alter the equation for TKE ($q^2/2$) from the classical superequilibrium SMC [Eq. (C1a)] to get

$$-\frac{\partial}{\partial z}\left[q\ell S_q\frac{\partial}{\partial z}\frac{q^2}{2}\right]=-\overline{w'u'}\frac{\partial\overline{u}}{\partial z}+\alpha g\overline{w'\theta'}-\frac{q^3}{B_1\ell}. \tag{13}$$

Variables used here are the same as defined in appendix C. The left-hand side of Eq. (13) represents the turbulent diffusion of TKE by using a diffusivity that is proportional to the product of turbulent velocity scale q and length scale ℓ with constant S_q = 0.2 (Mellor and Yamada 1982). On the right-hand side are the shear production, buoyancy production (destruction) and dissipation of TKE. Technically, Eq. (13) no longer indicates a superequilibrium state, so we will refer to it as "super-equilibrium," since it is still a simplified version of the original wave breaking model. Assuming dissipation is constant in the wave breaking layer ($|z| < z_0$, z_0 is the roughness scale), the scaling of Terray et al. (1996) argues that about half of the wave energy input is dissipated in the breaking layer; the other half is transported downward via turbulent diffusion. Thus, the upper boundary condition for Eq. (13) is

$$q\ell S_q\frac{\partial}{\partial z}\frac{q^2}{2}=\frac{1}{2}\alpha_b u_*^3,\quad \text{at}\quad z=-z_0, \tag{14}$$

where the coefficient α_b is commonly regarded as a function of sea state (Drennan et al. 1992). However, for well-developed waves, its dependence on sea state is so weak that one can treat it as a constant of order 100. For simplicity, 100 is used here, and we also require the energy flux due to breaking waves approaches zero as depth increases.

By defining a strained coordinate

$$y=\int_{-z_0}^{z}\frac{dz'}{\ell}=\frac{1}{\kappa}\ln\frac{-z_0}{z}, \tag{15}$$

where ℓ has been assumed to be $\kappa|z|$, and applying the surface layer approximations [Eqs. (C3a), (C3g), (C3i)], Eq. (13) can be reorganized into

$$\frac{\partial^2}{\partial y^2}q^3-\frac{3}{B_1S_q}q^3=\frac{-3u_*^3}{S_q}(\phi_m-\zeta). \tag{16}$$

As the second-order derivative of $(\phi_m-\zeta)$ in the surface layer is quite small, the analytical solution for Eq. (16) can be approximated as

$$q^3=u_*^3[B_1(\phi_m-\zeta)+c\xi^{-n}], \tag{17}$$

with a new parameter $\xi=|z|/z_0$, and constants $c=(1/2)\alpha_b\sqrt{3B_1/S_q}$ and $n=\sqrt{3/B_1S_q\kappa^2}$. Replacing Eq. (36a) in the classical superequilibrium SMC with the dimensionless form of Eq. (17), we arrive at a set of nondimensional equations that includes the effects of wave breaking:

$$q^{*3}=B_1(\phi_m-\zeta)+c\xi^{-n}, \tag{18a}$$

$$\frac{1}{3A_1q^*}=\phi_m\left\{r-C_1-\frac{[6A_1+3A_2(1-C_2)]\zeta}{q^{*3}}\right\}-\phi_h\left[\frac{3A_2\zeta}{q^{*3}}\right], \tag{18b}$$

$$\frac{1}{3A_2q^*}=\phi_h\left\{r-\frac{[6A_1+B_2(1-C_3)]\zeta}{q^{*3}}\right\}. \tag{18c}$$

Using the trust-region dogleg algorithm (Powell 1970) implemented in MATLAB, Eqs. (18) are solved to predict ϕ_h as a function of ζ and ξ (Fig. 6a). This model considers extra TKE input from surface wave breaking, so its temperature scaling ϕ_h is additionally regulated by the distance from the depth of energy injection z_0. However, the influence of surface wave breaking is mainly confined in a shallow layer of thickness

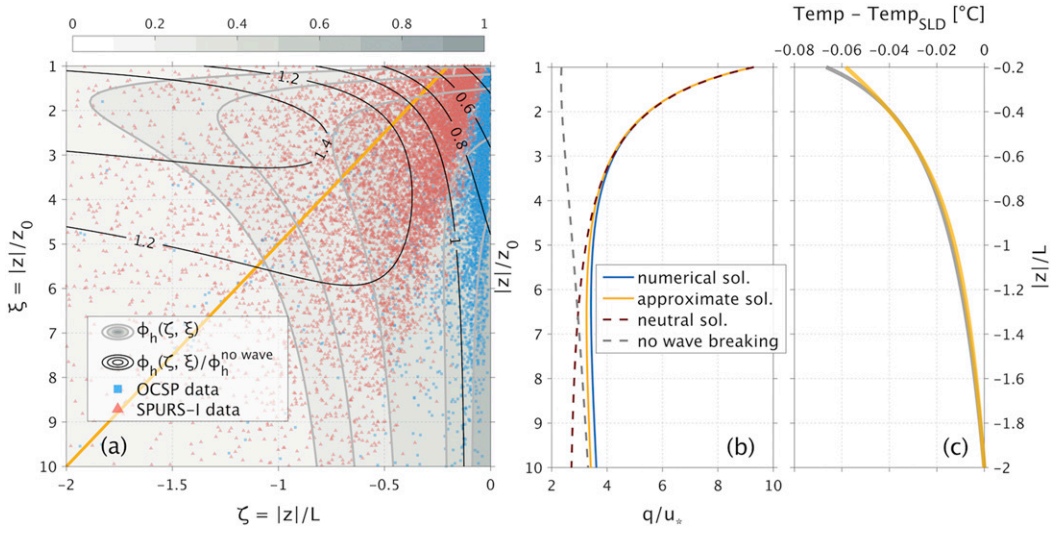

FIG. 6. (a) Variations of ϕ_h in the super-equilibrium (SE) wave breaking model (with $\ell = \kappa|z|$) where q^3 is approximated by Eq. (17). Color filled contours show the values of ϕ_h (0.22, 0.25, 0.3, 0.45, 0.6) predicted by the model. Black isolines show the ratios of the model-derived ϕ_h to those from the classical superequilibrium SMC (Kantha and Clayson, 1994) with no wave effects. The yellow line indicates the case ($z_0/L = 0.2$) plotted in (b) and (c). Observed parameter values at OCSP (blue) and SPURS-I (red) are overlaid. Roughness lengths are determined from significant wave heights with $z_0 = 0.6H_s$. (b) Turbulent velocity scale q in the SE wave breaking model when $z_0/L = -0.2$. Blue and yellow line show the numerical and approximate solution of Eq. (16), respectively. Brown and gray dash line show the solution in neutral limit (Craig 1996) and in case of no wave breaking, respectively. (c) Temperature (referenced to the value at the surface layer depth) profiles predicted by MOST (gray) and by the SE wave breaking model (yellow). Predictions are obtained by cumulatively integrating the predicted gradients with ϕ_h from Eqs. (3) (gray), and from the model (yellow) with $z_0/L = -0.2$, assuming $z_0 = 1.2$ m, 12-m surface layer depth and 10 m s^{-1} wind at 10-m height.

about $6z_0$. Compared to the scaling from the classical superequilibrium SMC (or MOST), the reduction of ϕ_h in the forced convection regime can be up to 60%, while the deviation from MOST gradually diminishes as the magnitude of ξ or ζ becomes larger. Enhancement of ϕ_h can also happen in stronger unstable conditions, and this model behavior is traced back to the reduced vertical TKE ratio $\overline{w'w'}/q^2$, or mixing efficiency, because dissipation exceeds production. Although we are not sure if this elevation of ϕ_h is physically realistic, it does not impact our test results for this wave breaking model (Fig. 8).

To assess the reliability of the approximate solution [Eq. (17)] used in the calculation of model ϕ_h, numerical solution of Eq. (16) is investigated with a fourth-order finite difference method (Kierzenka and Shampine, 2001), after substituting ϕ_m with an expression derived from Eqs. (18b) and (18c), and rewriting ζ as $e^{-\kappa y}z_0/L$. Figure 6b shows an example of the numerically solved $q^* = q/u_*$ when $z_0/L = -0.2$, along with solutions from Eq. (17), from the neutral limit (Craig 1996) and from the classical superequilibrium SMC without wave breaking. The approximate solution exactly coincides with the numerical solution near the surface, but gently converges to the classical solution at depth. Compared to the neutral solution of Craig (1996), the approximate solution agrees better with the numerical solution as buoyancy gradually becomes important at depth, and its advantage is even more prominent at larger $|z_0/L|$. Since the subtle differences between the numerical and approximate solution are found to have negligible impact on the resulting ϕ_h, and, given that the major parameter values observed here have $|z_0/L|$ smaller than 0.2, we may conclude that Eq. (17) is a sound approximation for the TKE under breaking waves, as modeled by Eq. (13). Therefore, the temperature scaling ϕ_h based on Eq. (17) should largely reflect the surface layer temperature predicted by the full model of Craig and Banner (1994).

b. *Similarity relations in Langmuir turbulence model*

Over the course of continuous efforts to include Langmuir turbulence in classical SMCs, until the recent model by Harcourt (2015), a series of modifications have been proposed: Governing equations are extended to incorporate the CL vortex force and other related terms (D'Alessio et al. 1998; Kantha and Clayson 2004); closure assumptions are generalized to have consistent dependency on Stokes drift (Harcourt 2013, 2015). As a result, the modified TKE equation has extra production by the CL vortex force, directly elevating the vertical TKE $\overline{w'w'}$. In addition, the inhomogeneous closures for the pressure-strain rate and pressure-scalar gradient correlations (Harcourt 2015) also redirect part of the CL vortex production into the crosswind direction to rectify the predictions of second-order statistics. Meanwhile, the inclusion of the CL vortex production in algebraic Reynolds stress model (ARSM) naturally entails a fundamentally different downgradient assumption for momentum fluxes:

$$\overline{w'\mathbf{u}'} = -K_m \frac{\partial \overline{\mathbf{u}}}{\partial z} - K_m^s \frac{\partial \mathbf{u}^s}{\partial z}, \tag{19}$$

where K_m is the conventional eddy viscosity, and K_m^s is a Stokes eddy coefficient. A similar assumption for momentum flux in the KPP scheme is also adopted in McWilliams et al. (2012).

With these and some other adjustments to parameterize Langmuir turbulence, the model of Harcourt (2015) showed promising agreements with LES results. Here we start from the superequilibrium version of Harcourt (2015), with the goal to attain similarity relations in a Langmuir turbulence-affected surface layer, provided the extra physics of Langmuir turbulence is properly represented in these model equations:

$$\frac{q^3}{B_1\ell} = -\overline{w'u'}\frac{\partial \overline{u}}{\partial z} - \overline{w'u'}\frac{\partial u^s}{\partial z} + \alpha g \overline{w'\theta'}, \tag{20a}$$

$$\overline{u'u'} = \frac{q^2}{3}\left(1 - \frac{6A_1}{B_1}\right) - \frac{6A_1\ell}{q}\left(\overline{w'u'}\frac{\partial u^s}{\partial z} f_z^s \cos^2\gamma + \overline{w'u'}\frac{\partial \overline{u}}{\partial z}\right), \tag{20b}$$

$$\overline{v'v'} = \frac{q^2}{3}\left(1 - \frac{6A_1}{B_1}\right) - \frac{6A_1\ell}{q}\overline{w'u'}\frac{\partial u^s}{\partial z} f_z^s \sin^2\gamma, \tag{20c}$$

$$\overline{w'w'} = \frac{q^2}{3}\left(1 - \frac{6A_1}{B_1}\right) - \frac{6A_1\ell}{q}\left[-\alpha g\overline{w'\theta'} + (1 - f_z^s)\overline{w'u'}\frac{\partial u^s}{\partial z}\right], \tag{20d}$$

$$\overline{w'u'} = \frac{-3A_1\ell}{q}\left[(\overline{w'w'} - C_1 q^2)\frac{\partial \overline{u}}{\partial z} - \alpha g\overline{u'\theta'} + (1 - f_z^s)\left(\overline{u'u'}\frac{\partial u^s}{\partial z} + \overline{u'v'}\frac{\partial v^s}{\partial z}\right) - \Pi_{13}^{(\mathrm{LCB})}\right], \tag{20e}$$

$$0 = \frac{-3A_1\ell}{q}\left[(\overline{w'w'} - C_1 q^2)\frac{\partial \overline{v}}{\partial z} - \alpha g\overline{v'\theta'} + (1 - f_z^s)\left(\overline{v'v'}\frac{\partial v^s}{\partial z} + \overline{u'v'}\frac{\partial u^s}{\partial z}\right) - \Pi_{23}^{(\mathrm{LCB})}\right], \tag{20f}$$

$$\overline{u'v'} = \frac{-3A_1\ell}{q}\left[\overline{w'u'}\frac{\partial \overline{v}}{\partial z} - 2\overline{w'u'}\frac{\partial u^s}{\partial z} f_z^s \cos\gamma \sin\gamma\right], \tag{20g}$$

$$\overline{u'\theta'} = \frac{-3A_2\ell}{q}\left[(1 - C_2)\overline{w'\theta'}\frac{\partial \overline{u}}{\partial z} + \overline{w'u'}\frac{\partial \overline{\theta}}{\partial z}\right], \tag{20h}$$

$$\overline{v'\theta'} = \frac{-3A_2\ell}{q}(1 - C_2)\overline{w'\theta'}\frac{\partial \overline{v}}{\partial z}, \tag{20i}$$

$$\overline{w'\theta'} = \frac{-3A_2\ell}{q}\left[\overline{w'w'}\frac{\partial \overline{\theta}}{\partial z} - (1 - C_3)\alpha g\overline{\theta'\theta'} + (1 - f_z^s)\left(\overline{u'\theta'}\frac{\partial u^s}{\partial z} + \overline{v'\theta'}\frac{\partial v^s}{\partial z}\right)\right], \tag{20j}$$

$$\overline{\theta'\theta'} = \frac{-B_2\ell}{q}\overline{w'\theta'}\frac{\partial \overline{\theta}}{\partial z}. \tag{20k}$$

In the equations above, variables inherited from the classical SMC represent the same quantities as in appendix C, to which are added u^s and v^s, Stokes drift in the downwind and crosswind directions, respectively. Angle γ denotes the orientation of the Langmuir cells (Van Roekel et al. 2012) relative to the y coordinate in a clockwise sense; $f_z^s = 1 + \tanh(0.25z/\ell^s)$ is a surface proximity function that decays with depth with a characteristic length scale

$$l^s = \frac{\displaystyle\int_{z_{\mathrm{PCL}^+}}^{0} \ell\left(-\overline{w'u'}\frac{\partial u^s}{\partial z}\right) dz}{\displaystyle\int_{z_{\mathrm{PCL}^+}}^{0} -\overline{w'u'}\frac{\partial u^s}{\partial z}\, dz}, \tag{21}$$

where $|z_{\mathrm{PCL}^+}|$ is the deepest depth at which the CL vortex production $(-\overline{w'u'}\partial u^s/\partial z)$ still remains positive. The term $\Pi_{ij}^{(\mathrm{LCB})}$ is the balancing component of the rapid pressure–strain rate closure designed to cancel the explicit dependence of K_m^s on the misalignment angle γ. A detailed expression for $\Pi_{ij}^{(\mathrm{LCB})}$ is provided in Harcourt (2015).

Note that the same boundary layer approximations have been applied in Eqs. (20), and the x coordinate is still chosen to align with the surface wind stress, though the surface wave direction may be misaligned. In the case of nonzero crosswind Stokes drift v^s, although crosswind stress $\overline{w'v'}$ is zero, $\partial\overline{v}/\partial z$ is not necessarily zero because the flux proportional to the Stokes shear must be compensated by that proportional to the Eulerian shear [see Eq. (19)]. Thus, covariance $\overline{w'v'}$, $\overline{u'v'}$, $\overline{v'\theta'}$ are retained in Eqs. (20). In the process of nondimensionalization, the downwind and crosswind components of Stokes shear can be scaled by introducing Stokes stability parameters

$$\eta^x = -\hat{\boldsymbol{\tau}}_w \cdot \frac{\dfrac{\partial \mathbf{u}^s}{\partial z}}{\dfrac{u_*}{\kappa|z|}}, \tag{22a}$$

$$\eta^y = -\hat{\mathbf{z}} \cdot \frac{\left(\hat{\boldsymbol{\tau}}_w \times \dfrac{\partial \mathbf{u}^s}{\partial z}\right)}{\dfrac{u_*}{\kappa|z|}}, \tag{22b}$$

where $\hat{\boldsymbol{\tau}}_w$ is the unit vector in the direction of surface wind stress and $\hat{\mathbf{z}}$ is the unit vector of the z coordinate. Note that η^x shares the sign convention of forcing parameter ζ, not of dimensionless shear ϕ_m. Following the procedure in appendix C, Eqs. (20) are nondimensionalized and reduced to

$$q^{*3} = B_1\ell^*(\phi_m^x - \zeta - \eta^x), \tag{23a}$$

$$\frac{1}{3A_1 q^*\ell^*} = \phi_m^x\left\{r - C_1 - \frac{[6A_1 + 3A_2(1 - C_2)]\zeta\ell^*}{q^{*3}} - \frac{12A_1\tilde{\eta}^x\ell^*}{q^{*3}}\right\} - \phi_h\left[\frac{3A_2\zeta\ell^*}{q^{*3}}\right] - \phi_m^y\left[\frac{3A_1\tilde{\eta}^y\ell^*}{q^{*3}}\right] - \tilde{\eta}^x r, \tag{23b}$$

$$\frac{1}{3A_2 q^*\ell^*} = \phi_h\left\{r - \frac{[6A_1 + B_2(1 - C_3)]\zeta\ell^*}{q^{*3}} - \frac{(6A_1 + 3A_2)\tilde{\eta}^x\ell^*}{q^{*3}}\right\} - \phi_m^x\left[\frac{3A_2(1 - C_2)\tilde{\eta}^x\ell^*}{q^{*3}}\right] - \phi_m^y\left[\frac{3A_2(1 - C_2)\tilde{\eta}^y\ell^*}{q^{*3}}\right], \tag{23c}$$

$$0 = \phi_m^y\left\{r - C_1 - \frac{[6A_1 + 3A_2(1 - C_2)]\zeta\ell^*}{q^{*3}} - \frac{9A_1\tilde{\eta}^x\ell^*}{q^{*3}}\right\} - \tilde{\eta}^y r, \tag{23d}$$

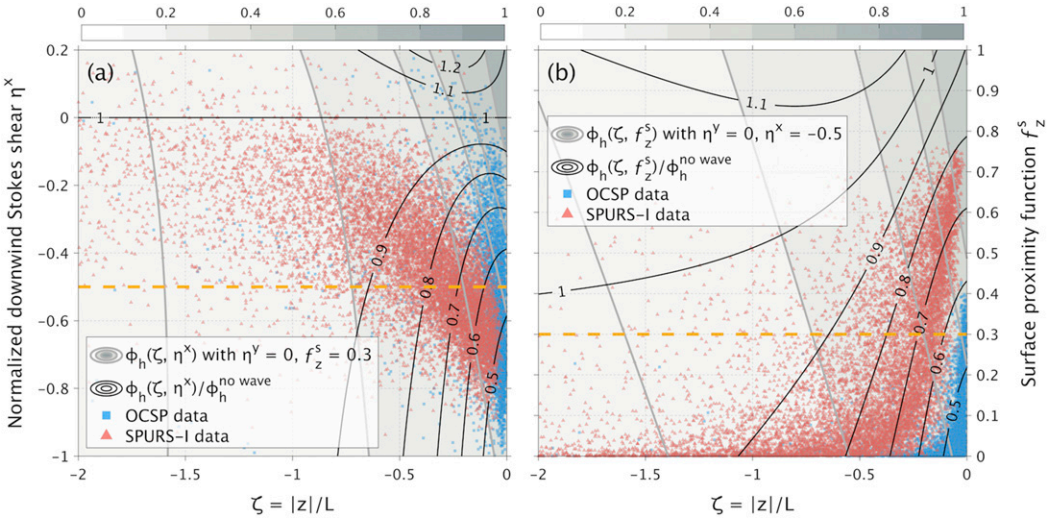

FIG. 7. Dimensionless temperature gradient ϕ_h predicted by the superequilibrium Langmuir turbulence model (Harcourt 2015, $\ell = \kappa|z|$). (a) Variations of the model-derived ϕ_h as a function of ζ and η^x when the normalized crosswind Stokes shear $\eta^y = 0$ and the surface proximity function $f_z^s = 0.3$. (b) Variations of the model-derived ϕ_h as a function of ζ and f_z^s when $\eta^y = 0$ and $\eta^x = -0.5$. In both (a) and (b), color filled contours show the values of ϕ_h (0.15, 0.2, 0.3, 0.4, 0.5, 0.7) predicted; black isolines show the ratios of the model-derived ϕ_h to those from the classical superequilibrium SMC (Kantha and Clayson 1994) with no wave effects; yellow dash line shows the constant parameter value selected in the other panel. Observed parameter values at OCSP (blue) and SPURS-I (red) are overlaid.

where ϕ_m^x and ϕ_m^y are dimensionless gradients of mean Eulerian velocity in the downwind $\overline{u}$ and crosswind $\overline{v}$ directions, and the prefactor $(1 - f_z^s)$ has been absorbed into the Stokes stability parameters in Eqs. (23b)–(23d), so that $\tilde{\eta}^x = (1 - f_z^s)\eta^x$, $\tilde{\eta}^y = (1 - f_z^s)\eta^y$.

In the surface layer, we use the classical mixing length argument that $\ell^* \equiv \ell/\kappa|z| = 1$. A more dynamical determination of length scale will be discussed later in section 3c. Making use of the same algorithm, we solve Eqs. (23) to express ϕ_h as a function of ζ, η^x, η^y, and f_z^s. For situations when the wind and waves are aligned ($\eta^y = 0$), a map of the model-derived ϕ_h in ζ and η^x space (Fig. 7a) with $f_z^s = 0.3$, which is a typical value of estimated f_z^s from observations, shows this model predicts a smaller temperature scaling ϕ_h than the classical superequilibrium SMC (or MOST), when the Stokes drift shear is in downwind direction ($\eta^x < 0$). The reduction of ϕ_h generally increases as the magnitude of η^x gets larger, but the modification of ϕ_h by Langmuir turbulence only seems to be significant when convection is weak. The smaller ϕ_h in this model is physically related to the enhanced vertical TKE and the additional contribution to vertical heat flux from horizontal heat flux [Eqs. (20d), (20j)], both due to the CL vortex force. This model also predicts larger ϕ_h than the classical superequilibrium SMC (or MOST) when $\eta^x > 0$, implying intensified unstable thermal gradient when Stokes drift is in the opposite direction of the wind, however, this rarely occurs. Note that the model prediction of ϕ_h is also set by the surface proximity function, and such dependence of ϕ_h on f_z^s when $\eta^x = -0.5$ is demonstrated in Fig. 7b. As the surface proximity function effects a local redistribution between components of Reynolds stress production, higher values normally decrease the contribution of the CL vortex production to the vertical TKE and vertical fluxes, leading to weaker reduction of ϕ_h by Langmuir turbulence. Similarly, the model-derived ϕ_h is sensitive to f_z^s values in weakly convective regime.

c. Comparison of model results with observations

The analyses of model behaviors under idealized forcing (Figs. 6a and 7) clearly show that both surface wave breaking and Langmuir turbulence can modify the temperature scaling, and the temperature gradient is additionally regulated by wave forcing parameters. As a further comparison with observations needs realistic wave forcing parameters, we estimate them from available observations.

The calculation of ξ assumes the roughness length scale $z_0 = 0.6H_s$ (Terray et al. 1996), where the coefficient 0.6 is admittedly uncertain, but the proportionality with H_s is supported by previous studies (Duncan 1981; Zippel et al. 2018). Stokes stability parameters η^x and η^y are specified by the vertical shear of Stokes drift according to Eqs. (22). The surface proximity function f_z^s has a decay scale l^s that is not easily quantifiable. Hence in Eq. (21), we use a linear profile of momentum flux, $\overline{w'u'} = -u_*^2(1 + z/H)$, and assume a parabolic profile of length scale, $\ell = \kappa|z|(1 + z/H)$, in the OSBL. Typical values for l_s are about 0.3 and 0.7 m at OCSP and SPURS-I, respectively, generally smaller than the effective e-folding depth scale [approximately $0.14U_{10}^2/g$, per Harcourt and D'Asaro (2008)] of equilibrium waves.

The computed forcing parameters are laid out in Figs. 6a and 7. On the ζ axis, most of the data are in the forced convection regime, and the data from SPURS-I span a wider range than OCSP. On the ξ axis, measurements mostly occurred within a

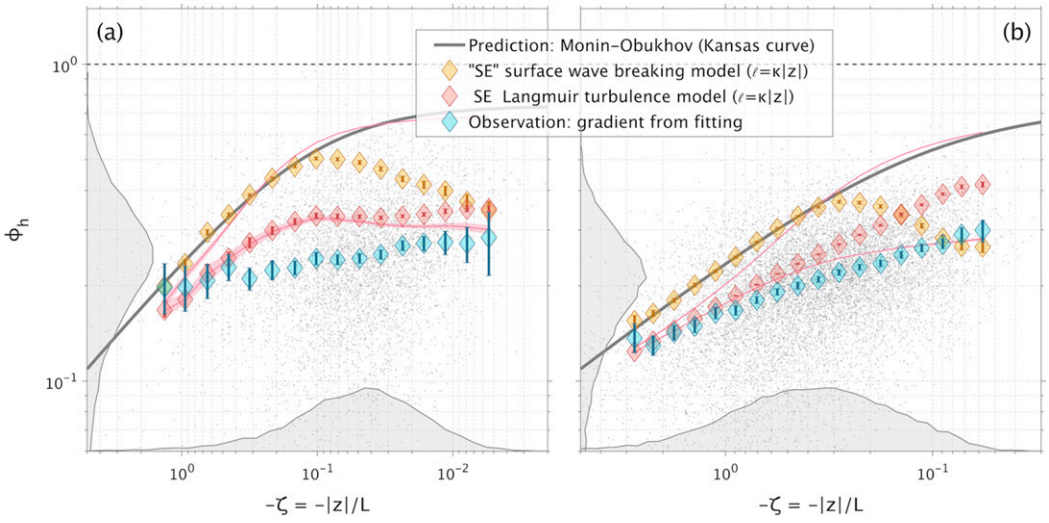

FIG. 8. Comparison of the superequilibrium (SE) model predictions of dimensionless gradient ϕ_h with observations at (a) OCSP and (b) SPURS-I. Only data from quasi-steady periods are presented. Model predictions are evaluated from Eqs. (18) and (23), using realistic forcing parameters. Observations of ϕ_h (gray dots) are the same as those in Fig. 5. Probability density functions of the observed values of $\log_{10}(\phi_h)$ and $\log_{10}(-\zeta)$ are shown by gray shadings on the left and bottom. Diamonds represent bin averages of observations and model predictions (see legend and text). The bin averages of observations also include some negative values (0.35% of total), though not shown in the log–log plot. Red lines are averages of predictions from the SE Langmuir turbulence model (Harcourt 2015, $\ell = \kappa|z|$) with constant surface proximity function $f_z^s = 1$ (upper) and $f_z^s = 0$ (lower). Confidence intervals (95%) of bin averages are indicated by error bars and shadings around red lines. The empirical relationship [Eq. (3b)] from the Kansas experiment (Businger et al. 1971) is displayed as the thick gray curve.

distance of $7z_0$ below the wave breaking layer. Though highly scattered, linear relationships with varying slopes (z_0/L) between ζ and ξ stand out prominently, owing to the nearly constant Obukhov length L in unstable conditions. In general, OCSP has smaller z_0/L values than SPURS-I (Fig. 6a). The Stokes drift shear is mostly in the destabilizing downwind direction, indicated by negative η^x and much smaller η^y (not shown). Given a similar depth for the shallowest sensor at both sites, the higher tip of SPURS-I data in Fig. 7b suggests relatively larger decay lengths for f_z^s there.

Model predictions of ϕ_h in the case of wave breaking and Langmuir turbulence are computed with realistic forcing parameters. The aggregated results are displayed in Fig. 8, together with the observations from section 2. The superequilibrium wave breaking model basically gives ϕ_h similar to the Kansas curve, except at relatively small $|\zeta|$. This is consistent with the example given in Fig. 6c, where ϕ_h are integrated to show the difference between temperature profiles predicted by the super-equilibrium wave breaking model and by MOST. The peak in the model-derived ϕ_h curve occurs because the observed forcing parameters (ζ, ξ) go through a ridge in the ϕ_h contours (Fig. 7a). Different constants in the roughness length formula, from 0.3 to 1.2, have been tested, yet the resulting ϕ_h curves have essentially the same shape, although the location of inflection differs a bit. In all, it seems that the simplified wave breaking model predicts reduced ϕ_h only in near-surface region, where $|\zeta|$ is relatively small. Considering the ϕ_h reduction is observed over a broader ζ range, there is insufficient evidence to support the first hypothesis that surface wave breaking is the main cause of the observed weak temperature gradients.

For the superequilibrium Langmuir turbulence model, predictions generally follow the trend of observations. At large $|\zeta|$, the model agrees well with observations, but as $|\zeta|$ becomes smaller, its prediction gradually deviates from observations, shifting toward the Kansas curve. Considering uncertainties in the estimate of the surface proximity function, we test the model with two bounding values, 0 and 1, of f_z^s. The test with $f_z^s = 1$, effectively a super-equilibrium version of Kantha and Clayson (2004), gives almost the same prediction as the Kansas curve. On the other hand, the test with $f_z^s = 0$, a slightly modified superequilibrium version of Harcourt (2013), gives result that roughly matches observations, except some deviations at OCSP. These two tests enclose all the variations of ϕ_h caused by the uncertainties of f_z^s in this model. Their convergence at large negative values of ζ is consistent with the fact that the variation of f_z^s does not change ϕ_h much at larger $|\zeta|$ (Fig. 7b). In all, the simplified Langmuir turbulence model can predict reduced ϕ_h over a ζ range similar to that observed, and makes robust ϕ_h predictions in relatively strong unstable conditions. However, its predictions in relatively weak unstable conditions are obscured by the uncertainties of the f_z^s estimation.

Previous LES studies on Langmuir turbulence have reported near-surface turbulent length scales different than $\kappa|z|$ (e.g., Harcourt 2013). The fact that we prescribed $\ell = \kappa|z|$ in Eqs. (23) may alter the superequilibrium model's predictive power, given that its full version uses a prognostic equation to determine ℓ. To further explore the possible impact of varying

ℓ^*, we add a $q^2\ell$ equation to the superequilibrium Langmuir model (following Kantha and Clayson 2004),

$$-\frac{\partial}{\partial z}\left(q\ell S_\ell \frac{\partial q^2\ell}{\partial z}\right) = E_1\ell\left(-\overline{w'u'}\frac{\partial \overline{u}}{\partial z}\right) + E_6\ell\left(-\overline{w'u'}\frac{\partial u^s}{\partial z}\right) + E_3\ell(\alpha g\overline{w'\theta'}) - \frac{E_2q^3}{B_1}\left(1+\frac{E_4\ell^2}{\kappa^2|z|^2}\right). \tag{24}$$

This equation is solely patterned after the full TKE equation but with tendency and advection terms omitted. On the right-hand side of Eq. (24) are shear production, CL vortex production, buoyancy production (destruction) and dissipation of $q^2\ell$, respectively. A wall-proximity term with coefficient E_4 is traditionally lumped together with dissipation to ensure $\ell = \kappa|z|$ near a bounding surface (Mellor and Yamada 1982). The term on the left-hand side of Eq. (24) represents down-the-gradient diffusion of $q^2\ell$, and it is not negligible in the surface layer as ℓ varies with depth. This departure from strict superequilibrium assumptions is necessary to retain the law-of-the-wall asymptotic behavior for vanishing Stokes drift when including the length scale equation (Kantha and Clayson 2004). For the values of constants in Eq. (24), Mellor and Yamada (1982) recommended $S_\ell = 0.2$, $E_1 = E_3 = 1.8$, $E_2 = 1$, $E_4 = 1.33$. Various values have been suggested for E_6 (Kantha and Clayson, 2004; Carniel et al. 2005; Kantha et al. 2010), and Harcourt (2015) settled at $E_6 = 6$. Applying the same scaling arguments as those in section 3b, we can nondimensionalize Eq. (24) to

$$-B_1S_\ell q^{*3}(\kappa\ell^*)^2 = B_1\ell^*(E_1\phi_m - E_3\zeta - E_6\eta^x) - E_2q^{*3}(1+E_4\ell^{*2}). \tag{25}$$

Supplementing Eqs. (23) with Eq. (25), we can solve for ϕ_h without invoking the assumption for ℓ^*. While we retain the standard model constants following Mellor and Yamada (1982), we find the resultant ϕ_h sensitive to the coefficient E_6 that regulates the CL vortex production of $q^2\ell$. The suggested value ($E_6 = 6$) actually gives too small ϕ_h over most of the observed ζ range (Figs. 9a,b), due to seemingly too large ℓ^* overall (maximum is about 3). The optimal value of E_6 that produces results most similar to observations is about 2.5. In this simplified model, the necessity of using a E_6 different than that of the full model (Harcourt 2015) may be linked to the negligence of turbulence transport in the TKE equation and the assumption of weak depth dependence of q^2 in the $q^2\ell$ equation. Other possible reasons may be rooted in the closure assumptions for the pressure–strain rate correlations, for which alternative formulations have been proposed by Pearson et al. (2019).

With $E_6 = 2.5$, the corresponding ℓ^* variations produced by tuning for model–observation agreement are shown in Figs. 9c and 9d. When the Stokes drift shear is downwind, the model predicts a length scale greater than $\kappa|z|$ and the enhancement of ℓ^* is more profound in weakly unstable conditions, with ℓ^* approaching 1.5 in nearly neutral conditions. In strongly unstable conditions, the influence of Stokes drift declines and ℓ reverts to the classical $\kappa|z|$ scaling. These are broadly consistent with the fact that Langmuir cells are indeed large-scale structures, and in line with the speculation that vigorous convection outcompetes Langmuir turbulence in strong cooling events (Li and Fox-Kemper 2017). Despite the empiricism involved here, the success of this enhanced superequilibrium Langmuir model in reproducing the mean scaling behavior of observations, and the reasonable underlying length scale variations, both serve to increase confidence in Langmuir turbulence as the major process responsible for reducing the near-surface temperature gradients. Note that our results for Langmuir model generally contradict previous findings from tuning model to LES solutions (Harcourt 2013, 2015). Here we need to either use fixed length scale ($\kappa|z|$) and turn off surface proximity function ($f_z^s = 0$), or use dynamical determination of length scale with a different E_6 constant and retain default surface proximity function to achieve better consistency with observations.

4. Summary

In this study, we find that in the unstable oceanic surface layer, MOST fails to quantitatively predict the mean thermal stratification from surface fluxes. Observations consistently present temperature gradients smaller than those suggested by MOST. As the thermal diffusivity K_h is related to the dimensionless temperature gradient ϕ_h through Eq. (4), smaller ϕ_h also means larger K_h and more efficient vertical heat transport.

To further investigate the cause of the theory–observation discrepancies, two hypotheses are considered. The first one attributes the weak temperature gradients to the effects of surface wave breaking, while the second one considers Langmuir turbulence as the major contributor. Although imperfect, PBL models that include the effects of surface wave breaking (Craig and Banner 1994) and Langmuir turbulence (Harcourt 2015) are taken to represent these two hypotheses, respectively. Each is tested in the framework of superequilibrium SMC (''level 2'' in Mellor and Yamada 1982), where model equations are reduced to give predictions of ϕ_h. It appears that the simplified surface wave breaking model can only give results partially matching with observations in weakly unstable conditions. In contrast, predictions from the simplified Langmuir turbulence model are very similar to observations across a broad stability range. When supplemented by a length scale equation, the simplified Langmuir turbulence model can quantitatively reproduce the mean scaling behavior of observations if a model constant in the length scale equation is appropriately tuned. Hence we conclude first, that there is not enough evidence to support the surface wave breaking as the main cause of the weak temperature gradients observed; second, that the observed weak temperature gradients are more likely due to Langmuir turbulence.

We have evaluated several approaches to combine the wave breaking and Langmuir turbulence parameterizations in one model, but none of these combined models gives better results than the Langmuir model alone. However, it is of significant concern that the downgradient diffusion assumption for TKE flux that leads to the S_q term in Eq. (13) is of uncertain validity when the CL vortex force interacts with the elevated TKE from

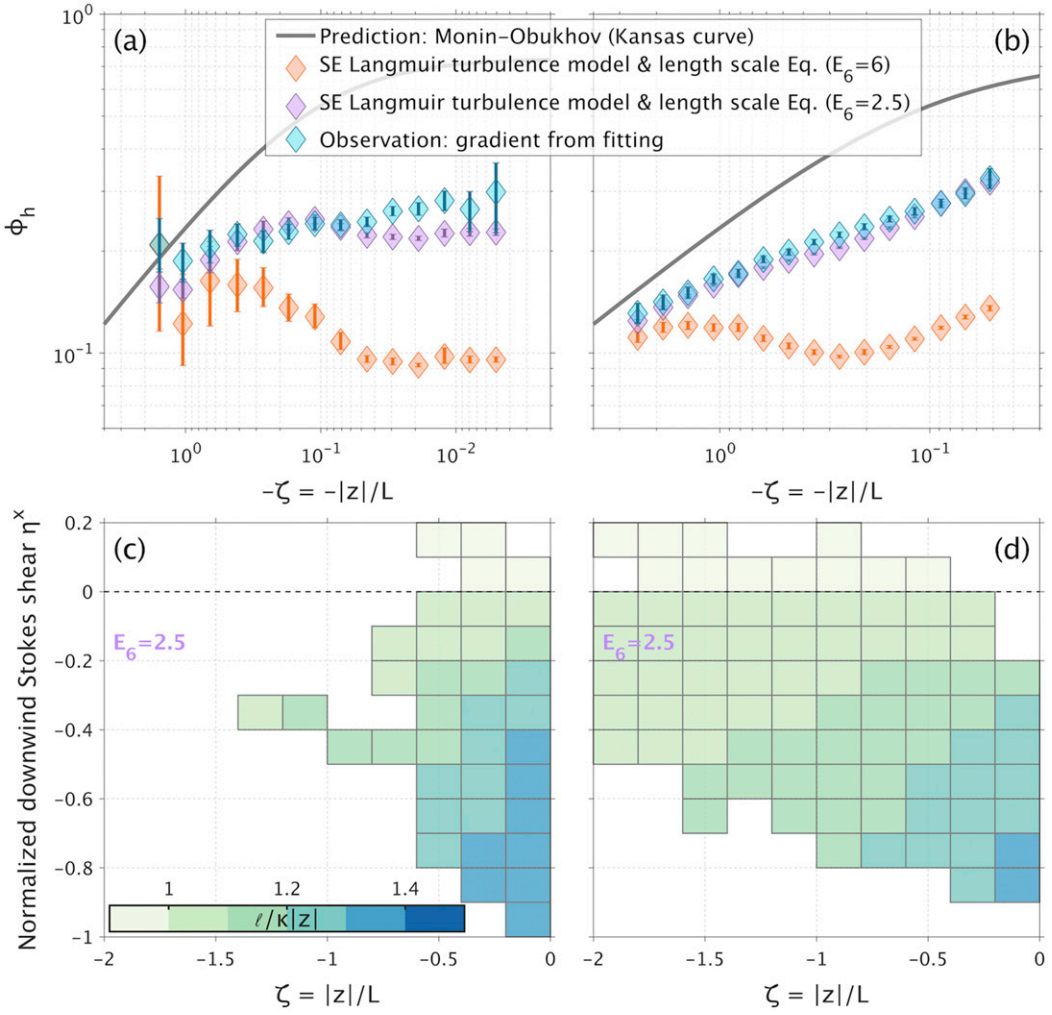

FIG. 9. (a) Comparison of Langmuir turbulence model predictions of ϕ_h with observations at OCSP. The model here uses dynamical length scale Eq. (24), rather than assuming $\ell = \kappa|z|$. Observations and MOST predictions of ϕ_h are copied from Fig. 8. Orange diamonds are averages of model predictions with $E_6 = 6$, as suggested by Harcourt (2015). Purple diamonds show averages of predictions from the same model, but tuning E_6 to 2.5 to best match observations. (b) As in (a), but use data from SPURS-I. (c) Variations of ℓ^* (length scale ℓ normalized by $\kappa|z|$) at OCSP as a function of ζ and η^x, as predicted by this Langmuir turbulence model with $E_6 = 2.5$. Predictions of ℓ^* are bin averaged and shown by the color of grids. Bins with less than 5 data points are ignored. (d) As in (c), but use data from SPURS-I.

wave breaking (see, e.g., Sullivan et al. 2007). These are issues that merit much more detailed study.

In the end, we allow that the data here may be insufficient to constrain all of the parameters in the models examined, and the conclusion of our hypotheses testing is by no means definitive. However, a combination of the data shown here and other observations will provide powerful constraints on models and theory designed to gain a physically realistic and quantitatively predictive understanding of the upper-ocean boundary layer.

Acknowledgments. We thank the OCS Project Office of NOAA/PMEL for collecting and distributing the OCSP mooring data. The surface wave data collection at OCSP was operated by Dr. Jim Thomson's team from APL-UW, with funding support from the National Science Foundation. Coastal Data Information Program (CDIP) provided the surface wave data curation for OCSP. CDIP is primarily supported by the U.S. Army Corps of Engineers. Data from the SPURS-I surface mooring were made available by Dr. J. Tom Farrar of the Woods Hole Oceanographic Institution. Support for the SPURS-I project was provided by NASA. This research was funded by the National Science Foundation (OCE1558459). Ramsey Harcourt was also supported in part by the Office of Naval Research (N00014-15-1-2308).

Data availability statement. Datasets analyzed in this article are openly available at locations cited in the reference section, with the exception of surface wave data at SPURS-I. A copy of

the original data and analysis scripts can be found in the Zenodo repository (http://doi.org/10.5281/zenodo.3988503).

APPENDIX A

Stokes Drift

The Stokes drift velocity in deep water (with dispersion relation $\omega^2 = gk$) is calculated by integrating the directional surface wave spectrum $S(f, \lambda)$ (Kenyon 1969),

$$\mathbf{u}^s(z) = 4\pi \int_0^{\infty} \int_{-\pi}^{\pi} f\mathbf{k} S(f,\lambda) e^{2kz} d\lambda \, df, \tag{A1}$$

where $\mathbf{k} = k\hat{\mathbf{k}} = k(-\sin\lambda\hat{\mathbf{x}} - \cos\lambda\hat{\mathbf{y}})$ is the horizontal wavenumber of surface waves; $\hat{\mathbf{x}}, \hat{\mathbf{y}}$ are unit vectors directing east and north; λ is the direction the wave is coming from (clockwise from true north); f and ω are the wave frequency in hertz and radian. The directional wave spectrum $S(f, \lambda)$ is estimated from archived records as

$$S(f,\lambda) = \frac{E(f)}{\pi}\left(\frac{1}{2} + a_1 \cos\lambda + b_1 \sin\lambda + a_2 \cos 2\lambda + b_2 \sin 2\lambda\right), \tag{A2}$$

in which a_1, b_1, a_2, b_2 are the normalized coefficients of directional Fourier series, and $E(f)$ is the nondirectional wave spectrum. Therefore, the east and north components of the Stokes drift velocity are

$$u^s = \frac{-16\pi^3}{g} \int_0^{\infty} f^3 E(f) \exp\left(8\pi^2 f^2 \frac{z}{g}\right) b_1 \, df, \tag{A3a}$$

$$v^s = \frac{-16\pi^3}{g} \int_0^{\infty} f^3 E(f) \exp\left(8\pi^2 f^2 \frac{z}{g}\right) a_1 \, df. \tag{A3b}$$

The resolved part of Stokes drift at OCSP (SPURS-I) are obtained by summing over the range from 0.025 (0.0325) to 0.58 (0.485) Hz with frequency bandwidths varying from 0.005 (0.005) Hz at low frequencies to 0.01 (0.02) Hz at high frequencies. For the unresolved part beyond cutoff frequency f_c, we use an analytical form that is consistent with the Phillips spectrum (Harcourt and D'Asaro 2008; Breivik et al. 2014),

$$S_{\mathrm{hf}} = S(f_c,\lambda)\left(\frac{f}{f_c}\right)^{-5}, \tag{A4}$$

in which the high-frequency tail is assumed to have the same directional distribution as the last resolved band. Then we can write the contribution from the spectral tail as

$$\mathbf{u}^s_{\mathrm{hf}}(z) = \frac{-16\pi^3 f_c^5}{g}\left[\frac{e^{-\mu f_c^2}}{f_c} - \sqrt{\mu\pi}\,\mathrm{erfc}(f_c\sqrt{\mu})\right] \times E(f_c)[b_1(f_c)\hat{\mathbf{x}} + a_1(f_c)\hat{\mathbf{y}}], \tag{A5}$$

with $\mu = -8\pi^2 z/g$. The vertical shear of the Stokes drift is computed by adding the vertical derivatives of the resolved part and the tail contribution, thus

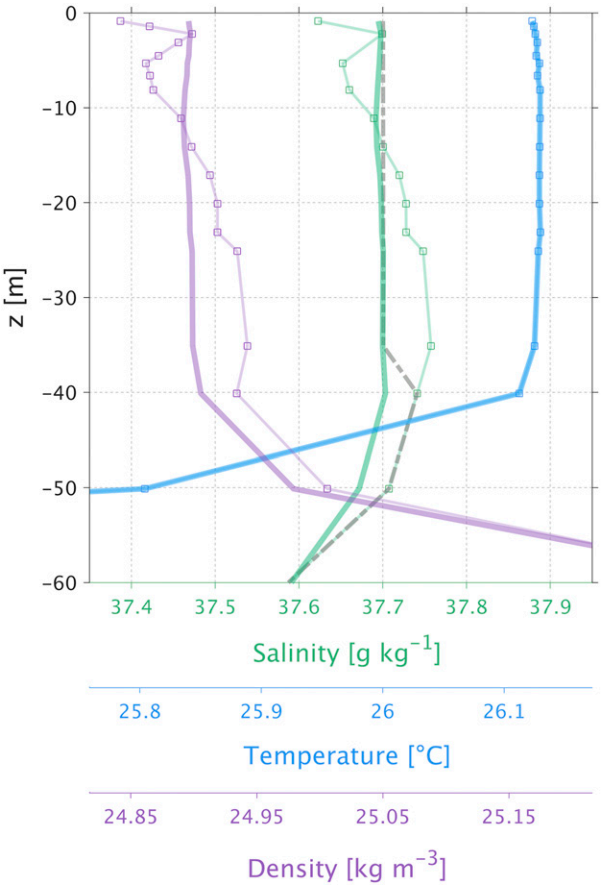

FIG. B1. Changes in salinity (green), temperature (blue), density (red) before (thin line with squares) and after (thick line) the salinity correction in SPURS-I dataset. Profiles are taken from 2230 local time 4 Aug 2013. The dash dotted gray line shows the nightly adjusted profile used to estimate sensor drift curves.

$$\frac{\partial \mathbf{u}^s}{\partial z}(z) = \frac{-128\pi^5}{g^2}\int_0^{f_c} f^5 E(f) \exp\left(8\pi^2 f^2 \frac{z}{g}\right)(b_1\hat{\mathbf{x}} + a_1\hat{\mathbf{y}})\, df - \frac{16\pi^3 f_c^5}{g}\sqrt{\frac{-2\pi^3}{gz}}\,\mathrm{erfc}(f_c\sqrt{\mu})E(f_c)[b_1(f_c)\hat{\mathbf{x}} + a_1(f_c)\hat{\mathbf{y}}]. \tag{A6}$$

APPENDIX B

Calibration of Salinity in SPURS-I Dataset

Although salinity profiles are not directly used to test the classical scaling, they are still important in setting upper ocean stratification. Unfortunately, salinity measurements from the SPURS-I mooring have shown consistent unrealistic variations in the OSBL. This is most evident during nighttime convection, as exampled by the raw profiles in Fig. B1. The upper ocean salinity variation is so large that it dominates the

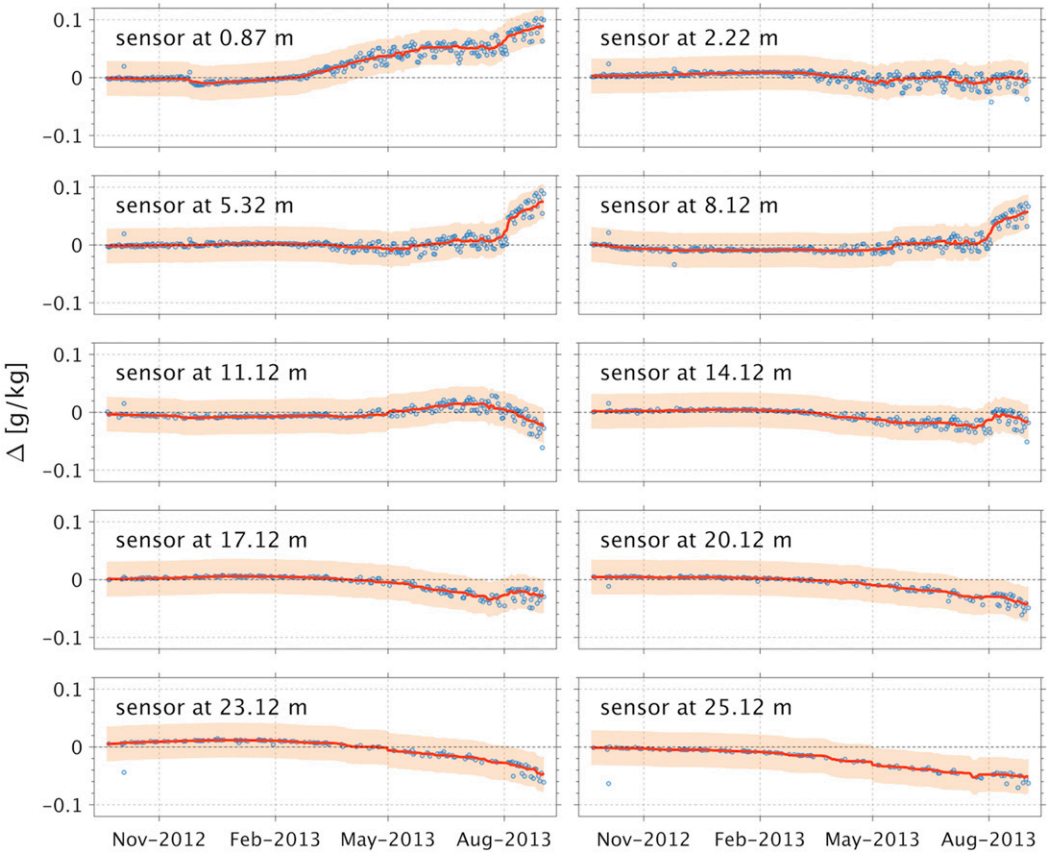

FIG. B2. Time series of salinity corrections (Δ = adjusted value − raw value) for the SPURS-I mooring sensors. Blue dots are sensor offsets estimated from the nightly corrections. Thick orange lines are drift curves derived from linear interpolations of the filtered nightly corrections. The light orange area shows $\pm 0.03\,\mathrm{g\,kg^{-1}}$ deviations from drift curves.

density structure, while the nearly homogeneous temperature profile indicates that the convective plume has resulted in a well-mixed layer. Therefore, we think these salinity jumps are probably due to biofouling or instrumental drift. To get a reasonable estimate of the boundary layer depth, it is necessary to adjust the raw salinity profiles to make the temperature–salinity structures consistent with expectations from convective mixing.

The method for salinity correction is to limit the range of salinity variation within the convective layer, defined as the extent to which the temperature exceeds a 0.006°C difference from the averaged temperature in upper 3 m, while still preserving the profile shape. Three steps are involved in this adjustment. First, salinity offset for each sensor in the convective layer is estimated once per night, in reference to the deepest, most well-mixed temperature profile with no rain event in the past 3 h. The maximum salinity variation (relative to the mean) allowed in the convective layer $|\Delta\overline{S}|_m$ is determined by the ratio between the magnitude of near-surface salt and heat fluxes, i.e.,

$$\frac{|\Delta\overline{S}|_m}{|\Delta\overline{\theta}|_{m,\mathrm{obs}}} = \frac{|\overline{w'S'}|_0|}{|\overline{w'\theta'}|_0|}, \tag{B1}$$

where $|\Delta\overline{\theta}|_{m,\mathrm{obs}}$ is the maximum of the measured temperature variation in the convective layer. The ratio of the maximum allowed $|\Delta\overline{S}|_m$ to the maximum measured $|\Delta\overline{S}|_{m,\mathrm{obs}}$ is used to downscale the salinity variation within the convective layer (Fig. B1). For each sensor adjusted, the salinity offset is recorded. Second, to avoid overcorrection, we only use the slow-varying drift curves extracted from the time series of nightly offsets. For sensor with adequate offset estimates, a 29-point median filter is used (Fig. B2). For sensor with only a few nightly offsets, a linear fit is used (not shown). Finally, to ensure the continuity of corrections, we interpolate these drift curves to hourly intervals before applying them to the raw salinity profiles. An example of the corrected salinity profile and the resulting density profile are shown in Fig. B1. The fact that almost all of the individual offset estimates are within the $\pm\ 0.03\,\mathrm{g\,kg^{-1}}$ deviation bands of drift curves indicates that the calibrations are well constrained.

APPENDIX C

Similarity Relations in the Classical Second Moment Closure

Here we show that the surface layer similarity relations can be independently derived from the classical superequilibrium SMC (Kantha and Clayson 1994), following the procedure

presented by Mellor (1973). A different derivation can be found in Cheng et al. (2002). To simplify presentation, we only consider the effect of potential temperature fluctuation θ' on buoyancy, though an extension to include salinity can be made easily. After applying the boundary layer approximations and directing the x coordinate to the direction of surface wind stress, the model equations can be simplified to

$$\frac{q^3}{B_1\ell} = -\overline{w'u'}\frac{\partial \overline{u}}{\partial z} + \alpha g\overline{w'\theta'}, \tag{C1a}$$

$$\overline{u'u'} = \frac{q^2}{3}\left(1 - \frac{6A_1}{B_1}\right) - \frac{6A_1\ell}{q}\overline{w'u'}\frac{\partial \overline{u}}{\partial z}, \tag{C1b}$$

$$\overline{v'v'} = \frac{q^2}{3}\left(1 - \frac{6A_1}{B_1}\right), \tag{C1c}$$

$$\overline{w'w'} = \frac{q^2}{3}\left(1 - \frac{6A_1}{B_1}\right) + \frac{6A_1\ell}{q}\alpha g\overline{w'\theta'}, \tag{C1d}$$

$$\overline{w'u'} = -\frac{3A_1\ell}{q}\left[(\overline{w'w'} - C_1q^2)\frac{\partial \overline{u}}{\partial z} - \alpha g\overline{u'\theta'}\right], \tag{C1e}$$

$$\overline{u'\theta'} = -\frac{3A_2\ell}{q}\left[\overline{w'u'}\frac{\partial \overline{\theta}}{\partial z} + (1 - C_2)\overline{w'\theta'}\frac{\partial \overline{u}}{\partial z}\right], \tag{C1f}$$

$$\overline{w'\theta'} = -\frac{3A_2\ell}{q}\left[\overline{w'w'}\frac{\partial \overline{\theta}}{\partial z} - (1 - C_3)\alpha g\overline{\theta'\theta'}\right], \tag{C1g}$$

$$\overline{\theta'\theta'} = -\frac{B_2\ell}{q}\overline{w'\theta'}\frac{\partial \overline{\theta}}{\partial z}. \tag{C1h}$$

In the above equations, $q^2 = \overline{u'u'} + \overline{v'v'} + \overline{w'w'}$ is twice the TKE; u', v', and w' are the three-dimensional velocity fluctuations in Cartesian coordinate system x, y, z; ℓ is the turbulent (master) length scale. Constants A_1 and C_1 were introduced in the approximations for the slow return to isotropy, and the rapid distortion components of the pressure–strain rate covariances, respectively (Rotta 1951; Crow 1968); constants A_2, C_2, and C_3 come from the approximations for the pressure–scalar gradient covariances (Mellor 1973; Andrén and Moeng 1993; Moeng and Wyngaard 1986; Launder 1975); constants B_1 and B_2 originate from the small-scale local isotropy hypothesis for the dissipation of TKE and temperature variance, respectively (Kolmogorov 1941). Standard values for these constants are listed below:

$$(A_1, A_2) = (0.92, 0.74); \tag{C2a}$$

$$(B_1, B_2) = (16.6, 10.1); \tag{C2b}$$

$$(C_1, C_2, C_3) = (0.08, 0.7, 0.2). \tag{C2c}$$

In the surface layer, vertical fluxes of momentum and heat may be approximated by their surface values, and other variables can be scaled accordingly:

$$(u_*^2, 0, Q) = -(\overline{w'u'}, \overline{w'v'}, \overline{w'\theta'}), \tag{C3a}$$

$$\ell^* = \frac{\ell}{\kappa|z|}, \tag{C3b}$$

$$(\overline{u^*u^*}, \overline{v^*v^*}, \overline{w^*w^*}) = \frac{(\overline{u'u'}, \overline{v'v'}, \overline{w'w'})}{u_*^2}, \tag{C3c}$$

$$(q^{*2}, \overline{u^*v^*}) = \frac{(q^2, \overline{u'v'})}{u_*^2}, \tag{C3d}$$

$$\overline{\theta^*\theta^*} = \frac{\overline{\theta'\theta'}}{\frac{Q^2}{u_*^2}}, \tag{C3e}$$

$$(\overline{u^*\theta^*}, \overline{v^*\theta^*}) = \frac{(\overline{u'\theta'}, \overline{v'\theta'})}{Q}, \tag{C3f}$$

$$\phi_m = \frac{\frac{\partial \overline{u}}{\partial z}}{\frac{u_*}{\kappa|z|}}, \tag{C3g}$$

$$\phi_h = \frac{\frac{\partial \overline{\theta}}{\partial z}}{\frac{Q}{\frac{u_*}{\kappa|z|}}}, \tag{C3h}$$

$$\zeta = \frac{|z|}{L} = \frac{\kappa|z|\alpha gQ}{u_*^3}. \tag{C3i}$$

With the scaling of variables defined above, the model equations can be nondimensionalized and reduced to

$$q^{*3} = B_1\ell^*(\phi_m - \zeta), \tag{C4a}$$

$$\frac{1}{3A_1q^*\ell^*} = \phi_m\left\{r - C_1 - \frac{[6A_1 + 3A_2(1 - C_2)]\zeta\ell^*}{q^{*3}}\right\} - \phi_h\left[\frac{3A_2\zeta\ell^*}{q^{*3}}\right], \tag{C4b}$$

$$\frac{1}{3A_2q^*\ell^*} = \phi_h\{r - [6A_1 + B_2(1 - C_3)]\zeta\ell^*/q^{*3}\}, \tag{C4c}$$

where $r = 1/3 - 2A_1/B_1$. The length scale ($q^2\ell$) equation is not included here, because for the classical superequilibrium SMC, the length scale equation can be simplified to give $\ell^* \approx 1$ (Kantha and Clayson 2004). Therefore, by assuming $\ell = \kappa|z|$ (i.e., $\ell^* = 1$), one can numerically solve Eqs. (C4) to express ϕ_m and ϕ_h as a function of ζ. These predictions of dimensionless gradients are referred to as the "model intrinsic similarity relations" in this paper. Previous studies have shown that the prediction of ϕ_h in this classical SMC matches the Kansas experimental data pretty well, especially under unstable conditions (see Fig. 2 of Kantha and Clayson 1994).

REFERENCES

Agrawal, Y. C., E. A. Terray, M. A. Donelan, P. A. Hwang, A. J. Williams, W. M. Drennan, K. K. Kahma, and S. A. Krtaigorodskii, 1992: Enhanced dissipation of kinetic energy beneath surface waves. *Nature*, **359**, 219–220, https://doi.org/10.1038/359219a0.

Anderson, N., J. Keene, and M. Cronin, 2018: Data acquisition and processing report for ocs mooring PA008. NOAA Data Rep.

PA008, NOAA/Pacific Marine Environmental Laboratory, 41 pp., https://www.pmel.noaa.gov/ocs/sites/default/files/atoms/files/OCS_DAPR_PA008_FINAL.pdf.

Andrén, A., and C.-H. Moeng, 1993: Single-point closures in a neutrally stratified boundary layer. *J. Atmos. Sci.*, **50**, 3366–3379, https://doi.org/10.1175/1520-0469(1993)050<3366:SPCIAN>2.0.CO;2.

Bouchard, P., and J. Farrar, 2008: Preliminary techniques for measuring waves on UOP buoys. Tech. Note, WHOI Upper Ocean Processes Group, Woods Hole Oceanographic Institution, 2 pp., https://uop.whoi.edu/techdocs/technote/TN-Feb08-WAMDAS.pdf.

Breivik, Ø., P. A. Janssen, and J. R. Bidlot, 2014: Approximate stokes drift profiles in deep water. *J. Phys. Oceanogr.*, **44**, 2433–2445, https://doi.org/10.1175/JPO-D-14-0020.1.

Burchard, H., 2001: Simulating the wave-enhanced layer under breaking surface waves with two-equation turbulence models. *J. Phys. Oceanogr.*, **31**, 3133–3145, https://doi.org/10.1175/1520-0485(2001)031<3133:STWELU>2.0.CO;2.

——, O. Petersen, and T. P. Rippeth, 1998: Comparing the performance of the Mellor-Yamada and the k-ε two equation turbulence models. *J. Geophys. Res.*, **103**, 10 543–10 554, https://doi.org/10.1029/98JC00261.

Businger, J. A., J. C. Wyngaard, Y. Izumi, and E. F. Bradley, 1971: Flux-profile relationships in the atmospheric surface layer. *J. Atmos. Sci.*, **28**, 181–189, https://doi.org/10.1175/1520-0469(1971)028<0181:FPRITA>2.0.CO;2.

Carniel, S., M. Sclavo, L. H. Kantha, and C. A. Clayson, 2005: Langmuir cells and mixing in the upper ocean. *IL Nuovo Cimento C*, **28**, 33–54, https://doi.org/10.1393/NCC/I2005-10022-8.

——, L. H. Kantha, J. W. Book, M. Sclavo, and H. Prandke, 2012: Turbulence variability in the upper layers of the Southern Adriatic Sea under a variety of atmospheric forcing conditions. *Cont. Shelf Res.*, **44**, 39–56, https://doi.org/10.1016/j.csr.2011.01.003.

Cheng, Y., V. M. Canuto, and A. M. Howard, 2002: An improved model for the turbulent PBL. *J. Atmos. Sci.*, **59**, 1550–1565, https://doi.org/10.1175/1520-0469(2002)059<1550:AIMFTT>2.0.CO;2.

Craig, P. D., 1996: Velocity profiles and surface roughness under breaking waves. *J. Geophys. Res.*, **101**, 1265–1277, https://doi.org/10.1029/95JC03220.

——, and M. L. Banner, 1994: Modeling wave-enhanced turbulence in the ocean surface layer. *J. Phys. Oceanogr.*, **24**, 2546–2559, https://doi.org/10.1175/1520-0485(1994)024<2546:MWETIT>2.0.CO;2.

Craik, A. D., and S. Leibovich, 1976: A rational model for Langmuir circulations. *J. Fluid Mech.*, **73**, 401–426, https://doi.org/10.1017/S0022112076001420.

Cronin, M. F., 2007: OCS Papa mooring in-situ hourly data. Updated daily, NOAA/Pacific Marine Environmental Laboratory, accessed 28 November 2019, https://www.pmel.noaa.gov/ocs/data/disdel/.

Crow, S., 1968: Turbulent Rayleigh shear flow. *J. Fluid Mech.*, **32**, 113–130, https://doi.org/10.1017/S0022112068000613.

D'Alessio, S. J. D., K. Abdella, and N. A. Mcfarlane, 1998: A new second-order turbulence closure scheme for modeling the oceanic mixed layer. *J. Phys. Oceanogr.*, **28**, 1624–1641, https://doi.org/10.1175/1520-0485(1998)028<1624:ANSOTC>2.0.CO;2.

D'Asaro, E. A., 2014: Turbulence in the upper-ocean mixed layer. *Annu. Rev. Mar. Sci.*, **6**, 101–115, https://doi.org/10.1146/annurev-marine-010213-135138.

——, J. Thomson, A. Y. Shcherbina, R. R. Harcourt, M. F. Cronin, M. A. Hemer, and B. Fox-Kemper, 2014: Quantifying upper ocean turbulence driven by surface waves. *Geophys. Res. Lett.*, **41**, 102–107, https://doi.org/10.1002/2013GL058193.

Deardorff, J. W., 1970: Convective velocity and temperature scales for the unstable planetary boundary layer and for Rayleigh convection. *J. Atmos. Sci.*, **27**, 1211–1213, https://doi.org/10.1175/1520-0469(1970)027<1211:CVATSF>2.0.CO;2.

de Boyer Montégut, C., G. Madec, A. S. Fischer, A. Lazar, and D. Iudicone, 2004: Mixed layer depth over the global ocean: An examination of profile data and a profile-based climatology. *J. Geophys. Res.*, **109**, C12003, https://doi.org/10.1029/2004JC002378.

Dijkstra, H. A., and G. Burgers, 2002: Fluid dynamics of El Niño variability. *Annu. Rev. Fluid Mech.*, **34**, 531–558, https://doi.org/10.1146/annurev.fluid.34.090501.144936.

Drennan, W. M., K. K. Kahma, E. A. Terray, M. A. Donelan, and S. A. Kitaigorodskii, 1992: Observations of the enhancement of kinetic energy dissipation beneath breaking wind waves. *Breaking Waves*, M. L. Banner and R. H. J. Grimshaw, Eds., Springer, 95–101.

——, M. A. Donelan, E. A. Terray, and K. B. Katsaros, 1996: Oceanic turbulence dissipation measurements in SWADE. *J. Phys. Oceanogr.*, **26**, 808–815, https://doi.org/10.1175/1520-0485(1996)026<0808:OTDMIS>2.0.CO;2.

Duncan, J. H., 1981: An experimental investigation of breaking waves produced by a towed hydrofoil. *Proc. Roy. Soc. London*, **377A**, 331–348, https://doi.org/10.1098/rspa.1981.0127.

Edson, J. B., C. J. Zappa, J. A. Ware, W. R. McGillis, and J. E. Hare, 2004: Scalar flux profile relationships over the open ocean. *J. Geophys. Res.*, **109**, C08S09, https://doi.org/10.1029/2003JC001960.

Emanuel, K., 2003: Tropical cyclones. *Annu. Rev. Earth Planet. Sci.*, **31**, 75–104, https://doi.org/10.1146/annurev.earth.31.100901.141259.

Fairall, C. W., E. F. Bradley, D. P. Rogers, J. B. Edson, and G. S. Young, 1996: Bulk parameterization of air-sea fluxes for tropical oceanglobal atmosphere coupled-ocean atmosphere response experiment. *J. Geophys. Res.*, **101**, 3747–3764, https://doi.org/10.1029/95JC03205.

——, ——, J. E. Hare, A. A. Grachev, and J. B. Edson, 2003: Bulk parameterization of air–sea fluxes: Updates and verification for the COARE algorithm. *J. Climate*, **16**, 571–591, https://doi.org/10.1175/1520-0442(2003)016<0571:BPOASF>2.0.CO;2.

Farrar, J. T., 2015: WHOI mooring CTD, surface flux and meteorological data for the SPURS-1 N. Atlantic field campaign, version 1. NASA Physical Oceanography Distributed Active Archive Center, accessed 18 June 2019, https://doi.org/10.5067/SPUR1-MOOR1.

——, and Coauthors, 2015: Salinity and temperature balances at the SPURS central mooring during fall and winter. *Oceanography*, **28**, 56–65, https://doi.org/10.5670/oceanog.2015.06.

Foken, T., 2006: 50 years of the Monin-Obukhov similarity theory. *Bound.-Layer Meteor.*, **119**, 431–447, https://doi.org/10.1007/s10546-006-9048-6.

Gargett, A. E., and J. R. Wells, 2007: Langmuir turbulence in shallow water. Part 1. Observations. *J. Fluid Mech.*, **576**, 27–61, https://doi.org/10.1017/S0022112006004575.

Garratt, J., 1992: *The Atmospheric Boundary Layer.* Cambridge Atmospheric and Space Science Series, Cambridge University Press, 316 pp.

Gerbi, G. P., J. H. Trowbridge, J. B. Edson, A. J. Plueddemann, E. A. Terray, and J. J. Fredericks, 2008: Measurements of momentum and heat transfer across the air–sea interface. *J. Phys. Oceanogr.*, **38**, 1054–1072, https://doi.org/10.1175/2007JPO3739.1.

Harcourt, R. R., 2013: A second-moment closure model of Langmuir turbulence. *J. Phys. Oceanogr.*, **43**, 673–697, https://doi.org/10.1175/JPO-D-12-0105.1.

——, 2015: An improved second-moment closure model of Langmuir turbulence. *J. Phys. Oceanogr.*, **45**, 84–103, https://doi.org/10.1175/JPO-D-14-0046.1.

——, and E. A. D'Asaro, 2008: Large-eddy simulation of Langmuir turbulence in pure wind seas. *J. Phys. Oceanogr.*, **38**, 1542–1562, https://doi.org/10.1175/2007JPO3842.1.

Högström, U., 1996: Review of some basic characteristics of the atmospheric surface layer. *Bound.-Layer Meteor.*, **78**, 215–246, https://doi.org/10.1007/BF00120937.

Jerlov, N., 1976: *Marine Optics*. Elsevier Oceanography Series, Vol. 14, Elsevier Scientific Publishing Company, 230 pp.

Kantha, L. H., and C. A. Clayson, 1994: An improved mixed layer model for geophysical applications. *J. Geophys. Res.*, **99**, 25 235–25 266, https://doi.org/10.1029/94JC02257.

——, and ——, 2004: On the effect of surface gravity waves on mixing in the oceanic mixed layer. *Ocean Modell.*, **6**, 101–124, https://doi.org/10.1016/S1463-5003(02)00062-8.

——, H. U. Lass, and H. Prandke, 2010: A note on Stokes production of turbulence kinetic energy in the oceanic mixed layer: Observations in the Baltic Sea. *Ocean Dyn.*, **60**, 171–180, https://doi.org/10.1007/s10236-009-0257-7.

Kenyon, K. E., 1969: Stokes drift for random gravity waves. *J. Geophys. Res.*, **74**, 6991–6994, https://doi.org/10.1029/JC074i028p06991.

Kierzenka, J., and L. F. Shampine, 2001: A BVP solver based on residual control and the MATLAB PSE. *ACM Trans. Math. Software*, **27**, 299–316, https://doi.org/10.1145/502800.502801.

Kolmogorov, A., 1941: The local structure of turbulence in incompressible viscous fluid for very large Reynolds numbers. *Dokl. Akad. Nauk SSSR*, **30**, 301–305.

Kukulka, T., A. J. Plueddemann, and P. P. Sullivan, 2012: Nonlocal transport due to Langmuir circulation in a coastal ocean. *J. Geophys. Res.*, **117**, C12007, https://doi.org/10.1029/2012JC008340.

——, ——, and ——, 2013: Inhibited upper ocean restratification in nonequilibrium swell conditions. *Geophys. Res. Lett.*, **40**, 3672–3676, https://doi.org/10.1002/grl.50708.

Langmuir, I., 1938: Surface motion of water induced by wind. *Science*, **87**, 119–123, https://doi.org/10.1126/science.87.2250.119.

Large, W. G., J. C. McWilliams, and S. C. Doney, 1994: Oceanic vertical mixing: A review and a model with a nonlocal boundary layer parameterization. *Rev. Geophys.*, **32**, 363–403, https://doi.org/10.1029/94RG01872.

Launder, B. E., 1975: On the effects of a gravitational field on the turbulent transport of heat and momentum. *J. Fluid Mech.*, **67**, 569–581, https://doi.org/10.1017/S002211207500047X.

LeMone, M. A., and Coauthors, 2019: 100 years of progress in boundary layer meteorology. *A Century of Progress in Atmospheric and Related Sciences: Celebrating the American Meteorological Society Centennial, Meteor. Monogr.*, No. 59, Amer. Meteor. Soc., https://doi.org/10.1175/AMSMONOGRAPHS-D-18-0013.1.

Li, Q., and B. Fox-Kemper, 2017: Assessing the effects of Langmuir turbulence on the entrainment buoyancy flux in the ocean surface boundary layer. *J. Phys. Oceanogr.*, **47**, 2863–2886, https://doi.org/10.1175/JPO-D-17-0085.1.

Lindstrom, E., F. Bryan, and R. Schmitt, 2015: SPURS: Salinity processes in the Upper-ocean regional study — The North Atlantic experiment. *Oceanography*, **28**, 14–19, https://doi.org/10.5670/oceanog.2015.01.

Lombardo, C. P., and M. C. Gregg, 1989: Similarity scaling of viscous and thermal dissipation in a convecting surface boundary layer. *J. Geophys. Res.*, **94**, 6273–6284, https://doi.org/10.1029/JC094iC05p06273.

Mahrt, L., 2014: Stably stratified atmospheric boundary layers. *Annu. Rev. Fluid Mech.*, **46**, 23–45, https://doi.org/10.1146/annurev-fluid-010313-141354.

McWilliams, J. C., P. P. Sullivan, and C.-H. Moeng, 1997: Langmuir turbulence in the ocean. *J. Fluid Mech.*, **334**, 1–30, https://doi.org/10.1017/S0022112096004375.

——, E. Huckle, J. H. Liang, and P. P. Sullivan, 2012: The wavy Ekman layer: Langmuir circulations, breaking waves, and Reynolds stress. *J. Phys. Oceanogr.*, **42**, 1793–1816, https://doi.org/10.1175/JPO-D-12-07.1.

Mellor, G. L., 1973: Analytic prediction of the properties of stratified planetary surface layers. *J. Atmos. Sci.*, **30**, 1061–1069, https://doi.org/10.1175/1520-0469(1973)030<1061:APOTPO>2.0.CO;2.

——, and T. Yamada, 1982: Development of a turbulence closure model for geophysical fluid problems. *Rev. Geophys.*, **20**, 851–875, https://doi.org/10.1029/RG020i004p00851.

Moeng, C.-H., and J. C. Wyngaard, 1986: An analysis of closures for pressure-scalar covariances in the convective boundary layer. *J. Atmos. Sci.*, **43**, 2499–2513, https://doi.org/10.1175/1520-0469(1986)043<2499:AAOCFP>2.0.CO;2.

Monin, A. S., and A. M. Obukhov, 1954: Basic laws of turbulent mixing in the surface layer of the atmosphere. *Tr. Geofiz. Inst., Akad. Nauk SSSR*, **24**, 163–187.

——, and A. Yaglom, 1971: *Statistical Fluid Mechanics: Mechanics of Turbulence*. Vol. 1, MIT Press, 769 pp.

Obukhov, A. M., 1946: Turbulence in thermally inhomogeneous atmosphere. *Tr. Inst. Teoret. Geofiz. Akad. Nauk SSSR*, **1**, 95–115.

Panofsky, H. A., 1963: Determination of stress from wind and temperature measurements. *Quart. J. Roy. Meteor. Soc.*, **89**, 85–94, https://doi.org/10.1002/qj.49708937906.

Paulson, C. A., and J. J. Simpson, 1977: Irradiance measurements in the upper ocean. *J. Phys. Oceanogr.*, **7**, 952–956, https://doi.org/10.1175/1520-0485(1977)007<0952:IMITUO>2.0.CO;2.

Pearson, B. C., A. L. Grant, J. A. Polton, and S. E. Belcher, 2015: Langmuir turbulence and surface heating in the ocean surface boundary layer. *J. Phys. Oceanogr.*, **45**, 2897–2911, https://doi.org/10.1175/JPO-D-15-0018.1.

——, ——, and ——, 2019: Pressure-strain terms in Langmuir turbulence. *J. Fluid Mech.*, **880**, 5–31, https://doi.org/10.1017/jfm.2019.701.

Powell, M. J. D., 1970: A FORTRAN subroutine for solving systems of nonlinear algebraic equations. *Numerical Methods for Nonlinear Algebraic Equations*, P. Rabinowitz, Ed., Gordon and Breach Science Publishers, 115–162.

Prandtl, L., 1925: Bericht über Untersuchungen zur ausgebildeten Turbulenz. *Z. Angew. Math. Mech.*, **5**, 136–139, https://doi.org/10.1002/zamm.19250050212.

Rodi, W., 1987: Examples of calculation methods for flow and mixing in stratified fluids. *J. Geophys. Res.*, **92**, 5305–5328, https://doi.org/10.1029/JC092iC05p05305.

Rotta, J., 1951: Statistische theorie nichthomogener turbulenz. *Z. Phys.*, **129**, 547–572, https://doi.org/10.1007/BF01330059.

Sallée, J. B., E. Shuckburgh, N. Bruneau, A. J. Meijers, T. J. Bracegirdle, and Z. Wang, 2013: Assessment of Southern Ocean mixed-layer depths in CMIP5 models: Historical bias and forcing response. *J. Geophys. Res.Oceans*, **118**, 1845–1862, https://doi.org/10.1002/jgrc.20157.

Shay, T. J., and M. C. Gregg, 1986: Convectively driven turbulent mixing in the upper ocean. *J. Phys. Oceanogr.*, **16**, 1777–1798,

https://doi.org/10.1175/1520-0485(1986)016<1777:CDTMIT>2.0.CO;2.

Simonot, J.-Y., and H. Le Treut, 1986: A climatological field of mean optical properties of the world ocean. *J. Geophys. Res.*, **91**, 6642–6646, https://doi.org/10.1029/JC091iC05p06642.

Skyllingstad, E. D., and D. W. Denbo, 1995: An ocean large-eddy simulation of Langmuir circulations and convection in the surface mixed layer. *J. Geophys. Res.*, **100**, 8501–8522, https://doi.org/10.1029/94JC03202.

Sullivan, P. P., and J. C. McWilliams, 2010: Dynamics of winds and currents coupled to surface waves. *Annu. Rev. Fluid Mech.*, **42**, 19–42, https://doi.org/10.1146/annurev-fluid-121108-145541.

——, ——, and W. K. Melville, 2007: Surface gravity wave effects in the oceanic boundary layer: Large-eddy simulation with vortex force and stochastic breakers. *J. Fluid Mech.*, **593**, 405–452, https://doi.org/10.1017/S002211200700897X.

Taylor, G., 1915: Eddy motion in the atmosphere. *Philos. Trans. Roy. Soc. London*, **215A**, 1–26, https://doi.org/10.1098/rsta.1915.0001.

Tejada-Martínez, A. E., and C. E. Grosch, 2007: Langmuir turbulence in shallow water. Part 2. Large-eddy simulation. *J. Fluid Mech.*, **576**, 63–108, https://doi.org/10.1017/S0022112006004587.

Terray, E., M. Donelan, Y. Agrawal, W. Drennan, K. Kahma, A. Williams, P. Hwang, and S. Kitaigorodskii, 1996: Estimates of kinetic energy dissipation under breaking waves. *J. Phys. Oceanogr.*, **26**, 792–807, https://doi.org/10.1175/1520-0485(1996)026<0792:EOKEDU>2.0.CO;2.

Thomson, J., 2019: Directional wave and sea surface temperature measurements collected in situ by Datawell Waverider buoys located near OCEAN STATION PAPA from 2010/06/16 to 2019/12/14, version 1. Coastal Data Information Program, SIO/UCSD, accessed 14 February 2020, http://cdip.ucsd.edu/themes/cdip?pb=1&u2=s:166:st:1&d2=p70.

Thorpe, S. A., 1984: The effect of Langmuir circulation on the distribution of submerged bubbles caused by breaking wind waves. *J. Fluid Mech.*, **142**, 151–170, https://doi.org/10.1017/S0022112084001038.

Van Roekel, L. P., B. Fox-Kemper, P. P. Sullivan, P. E. Hamlington, and S. R. Haney, 2012: The form and orientation of Langmuir cells for misaligned winds and waves. *J. Geophys. Res.*, **117**, C05001, https://doi.org/10.1029/2011JC007516.

von Kármán, T., 1931: Mechanische Ähnlichkeit und Turbulenz. *Proceedings of the Third International Congress on Applied Mechanics*, Vol. 1, Sveriges Litografiska Tryckerier, 85–93.

Wyngaard, J. C., 2010: *Turbulence in the Atmosphere*. Cambridge University Press, 393 pp.

Zedel, L., and D. Farmer, 1991: Organized structures in subsurface bubble clouds: Langmuir circulation in the open ocean. *J. Geophys. Res.*, **96**, 8889, https://doi.org/10.1029/91JC00189.

Zhang, C., 2005: Madden-Julian Oscillation. *Rev. Geophys.*, **43**, RG2003, https://doi.org/10.1029/2004RG000158.

Zippel, S. F., J. Thomson, and G. Farquharson, 2018: Turbulence from breaking surface waves at a river mouth. *J. Phys. Oceanogr.*, **48**, 435–453, https://doi.org/10.1175/JPO-D-17-0122.1.